



UNIVERSITÀ DEGLI STUDI DI PADOVA

Dipartimento di Fisica e Astronomia “Galileo Galilei”

Master Degree in Physics

Final Dissertation

Isospin symmetry in the fp-shell mirror nuclei

Thesis supervisor

Dr. Francesco Recchia

Thesis co-supervisor

Dr. Martha Liliana Cortés Sua

Candidate

Sara Pigliapoco

Academic Year 2019/2020

Contents

1	Introduction and theoretical framework	3
1.1	The Nuclear Shell model	5
1.1.1	The independent-particle model	6
1.2	The Isospin quantum number	6
1.3	Isospin breaking effects	8
2	Experimental Setup	11
2.1	The BigRIPS separator	14
2.2	The ZeroDegree spectrometer	16
2.3	Particle identification	16
2.3.1	The $B\rho$ measurement	16
2.3.2	The position measurement	17
2.3.3	The TOF measurement	18
2.3.4	The ΔE measurement	19
2.4	The DALI2+ array	20
3	Data analysis	23
3.0.1	Triggers	23
3.1	BigRIPS and ZeroDegree	25
3.1.1	PPAC and Focal Plane efficiencies	25
3.1.2	Plastic detectors	28
3.1.3	Ionization chambers	29
3.2	The PID	33
3.2.1	Charge States	41
3.2.2	Reactions	42
3.2.3	F3 vs F5 position distribution	43
3.3	DALI2+ calibration	47
3.3.1	Energy calibration	47
3.3.2	Time calibration	52
3.3.3	Background	53
3.4	Doppler-correction	54

3.4.1	Add-back procedure	55
4	Experimental results and discussion	57
4.1	Inclusive cross sections	57
4.2	Doppler-correction of γ -transitions	67
5	Conclusions	75
	Bibliography	79

Chapter 1

Introduction and theoretical framework

The atomic nucleus was discovered in 1911 by Ernest Rutherford [1] while he was testing the plum pudding model of the atom, proposed in 1904 by Thomson [2]. In this new model the nucleus is constituted by two different particles, protons and neutrons, bound together by the nuclear force in a system of dimensions of about 10^{-14} m.

Important theoretical efforts and experimental developments like discovery of the neutron, quantum theory, development of high energy accelerators allowed to accumulate information and understanding on the structure of the atomic nucleus.

One of the most important properties of nuclei is the existence of particularly stable nuclear configurations. These configurations are characterized by specific numbers of nucleons, which are called *magic numbers*, and the relative nuclei are *magic nuclei*. Many experimental evidences can be presented in support of the existence of these "magic" configurations. For example the proton(neutron) separation energy, $S_p(S_n)$, shows an increase in value when reaching these numbers of nucleons, which means that it is particularly difficult to remove a proton(neutron) from these configurations. The magicity is observed at the following numbers of nucleons: 2, 8, 20, 28, 50, 82 and 126.

Many different models have been developed, with the aim of describing the nuclear force, in order to reproduce and to predict the observed nuclear properties. One of these, the *Nuclear Shell model*, assumes that protons and neutrons occupy different orbits according to the Pauli Exclusion principle, in the same way as electrons do in the atoms. This model was first developed in 1934 by Elsasser [3] and Guggenheimer [4]. To reproduce nuclear orbits, they imposed that particles move in a central potential, but they were not able to predict the exact number of protons and neutrons to which these

particularly stable nuclear configurations correspond.

Different choices of central potential can be done. For example, using the Harmonic Oscillator Potential we obtain the harmonic oscillation occupancies at 2, 8, 20, 40, 70, 112, 168, etc [5]. These numbers largely deviate from the observed values and it is clear that something fundamental is still missing.

In 1949 separately Mayer [6] and Haxel, Jensen and Suess [7] were able to obtain the correct magic numbers by adding a spin-orbit term in the potential. In Figure 1.1 the chart of nuclides is presented. Magic numbers are also indicated together with half-lives.

A further step in the description of the nucleus was given by Heisenberg, who in 1932 proposed the concept of *isospin* [8], a new quantum number assigned to protons and neutrons. According to Heisenberg, protons and neutrons represent different states of the same particle, the nucleon. This statement is a natural consequence of the properties of charge-symmetry and charge-independence of the nuclear potential. The first symmetry implies that V_{nn} and V_{pp} are the same, or in other words that the interaction between protons is the same as that between neutrons. Charge-independence is even a stronger statement, because implies that $V_{pp}=V_{nn}=V_{pn}$. Assuming valid these symmetries, only the Coulomb force is responsible for the differences in the nuclear interaction, which can be manifested in properties such as the mass of the nucleus or the energy of its excited states. The study of mirror nuclei, which are nuclei with inverted numbers of protons and neutrons, is one of the most powerful tool to investigate those symmetries. In principle, neglecting the Coulomb interaction, energy levels of these pairs of nuclei should be the same. In the recent years instead, studies have shown that the electromagnetic interaction alone is not sufficient to account for levels splitting in these type of nuclei, reflecting the fact that other type of isospin non-conserving interaction may have to be considered.

In the present work, exotic nuclei near the proton drip line are studied, in particular isotopes like ^{56}Zn , ^{55}Cu and ^{56}Cu populated by knockout reactions. These are exotic proton-rich nuclei, but still not so far from the $N=Z$ line, that represent the best mass region to study isospin symmetry because protons and neutrons occupy the same orbitals. The *fp* shell has been historically the playground on which our understanding of nuclear structure and reactions could be challenged and developed.

We want to obtain new estimations on inclusive knockout cross-sections, for this particular reactions and also for other nuclei populated during the experiment, that can be further improved with the analysis of gamma radiation, which will be briefly introduced in the last part of this work. These results are important for further studies on the mirror energy differences, to investigate the mass dependence of the isospin-breaking effects and also

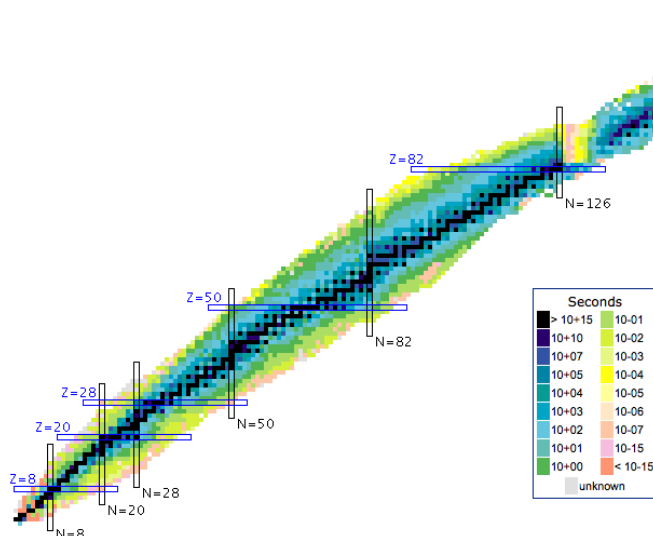


Figure 1.1: Chart of nuclides. Different colors represent half-lives, magic numbers are also reported.

to investigate to which extent weak binding and coupling to the continuum affect isospin.

1.1 The Nuclear Shell model

The Nuclear Shell model is one of the most robust model for nuclei close to the valley of stability. The nucleus is a many-body system, and its Hamiltonian can be written as the sum of the kinetic energy of each particle, plus the interaction between them:

$$\hat{H} = \sum_{i=0}^A -\frac{\hbar^2}{2m} \nabla_i^2 + \sum_{i<j}^A W(i, j) \quad (1.1)$$

where A is the number of the constituents of the nucleus, m is the mass of the nucleons, and $W(i, j)$ represent a two-body interaction term¹. Adding and subtracting an average potential U in equation (1.1), it is possible to rewrite the Hamiltonian as

$$\hat{H} = \left[\sum_{i=0}^A \left(-\frac{\hbar^2}{2m} \nabla_i^2 + U(i) \right) \right] + \left[\sum_{i<j}^A W(i, j) - \sum_{i=0}^A U(i) \right] = \hat{H}_0 + \hat{V}. \quad (1.2)$$

¹ It is possible to include also a three-body interaction term in the potential, but this is out of the scope of the present chapter.

In this way the nucleons are described as independent particle moving in an average potential U , created by all the particles which can be an harmonic oscillator, or a Woods-Saxon potential, plus a *residual interaction* V , that can be made small with a proper choice of U .

1.1.1 The independent-particle model

Neglecting for a moment V , we can solve the Schrödinger equation in the independent-particle model. For example if we choose the harmonic oscillator potential as the average potential, and adding the spin-orbit term, needed to reproduce the correct magic numbers, then U becomes [5]

$$U(r) = -U_0 + \frac{1}{2}m\omega^2r^2 - \frac{2}{\hbar^2}\alpha\hat{l} \cdot \hat{s}, \quad (1.3)$$

where \hat{l} and \hat{s} are the orbital angular momentum and the intrinsic spin operator respectively. Equation (1.3) can be rewritten using the total angular momentum operator \hat{j} , replacing

$$2\hat{l} \cdot \hat{s} = \hat{j}^2 - \hat{l}^2 - \hat{s}^2. \quad (1.4)$$

Solving the Schrödinger equation we find the single-particle spectrum, which is reported in Figure 1.2. In the right part of the picture is clearly visible the mixing of levels due to the spin-orbit force. This model give rise to spacing between certain energy levels, making possible to identify, in the vicinity of these gaps, closed shell configurations, which correspond to the magic numbers.

This work will be mostly concentrated on the analysis of nuclei belonging to the shell *fp* and proton rich, like ^{56}Zn and ^{55}Cu . They can be understood as an inert core of ^{40}Ca , plus valence nucleons.

1.2 The Isospin quantum number

The isospin is a quantum number that was introduced to explain some properties of the nuclear force. From the experiments, it has been shown, indeed, that to a good approximation the strong nuclear force does not distinguish between neutrons and protons², so it is possible to assign a vector, T , to the nucleons. The projections of this vector on an arbitrary chosen

² This symmetry is not valid anymore if we introduce the electromagnetic interaction, which can distinguish between neutrons and protons.

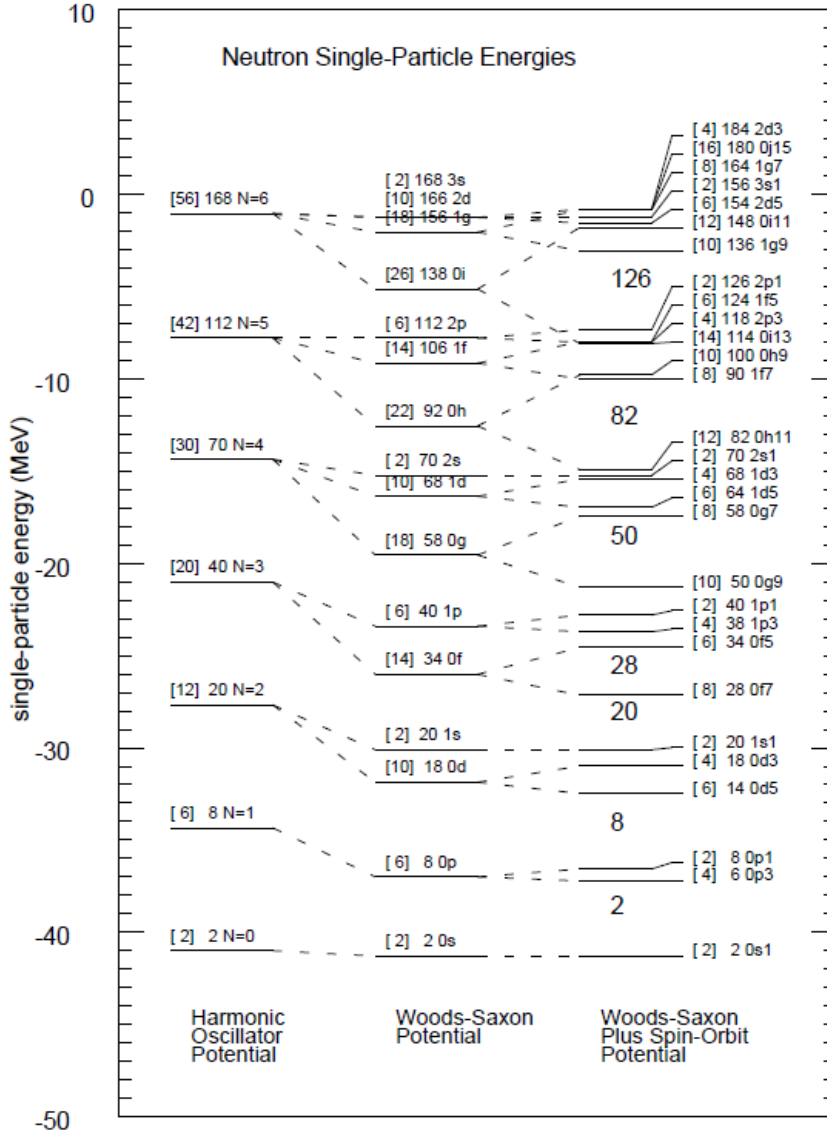


Figure 1.2: Single-particle spectrum obtained from different type of average potential: the harmonic oscillator (left), Woods-Saxon (center) and Woods-Saxon plus spin-orbit potential (right). Splitting of levels in the right part of the picture are due to the spin-orbit. Magic numbers are also reported.

z axis can be $\pm 1/2$ and they represent neutrons, $T_z = 1/2$, and protons³ $T_z = -1/2$. So if we take a nucleus made up of N neutrons and Z protons, it is possible to assign it a value of T_z in the following way [9]

$$T_z = \frac{N - Z}{2}. \quad (1.5)$$

Following the same formalism used for the other quantum numbers, energy levels in that nucleus can have isospin quantum number in the range

$$\left| \frac{N - Z}{2} \right| \leq T \leq \frac{N + Z}{2}. \quad (1.6)$$

For a given T we can define an *isobaric multiplet*, the set of nuclei with $T_z = T, T - 1, \dots, -T$, and the set of states with the same value of T in this multiplet is called *isobaric analogue states* (IAS).

If we neglect for a moment the Coulomb potential, looking at an isobaric multiplet, states with the same value of T occur at almost the same excitation energy relative to the ground state. This is a clear footprint of the *isospin symmetry* that characterizes the nuclear force. It is mainly the Coulomb force that lifts the degeneracy of isobaric analogue states, and it is particularly evident when comparing mirror nuclei. The difference in binding energies between the members of a multiplet is called Coulomb Displacement Energy (CDE). Actually it has been noticed experimentally that isospin breaking effects can not be completely explained by the presence of this electromagnetic interaction.

1.3 Isospin breaking effects

In the previous section we introduced the isospin quantum number as a consequence of the approximately charge-symmetry and charge-independence nature of the nuclear potential. At the end of the section it has been pointed out that the introduction of the Coulomb interaction between protons lifts the degeneracy of the IAS and also that this term alone can not explain the observed CDE between members of a multiplet. Even adding further contributions to the calculation of the CDE, like an exchange term related directly to the two-body force because of the Pauli exclusion principle, and a spin-orbit term as in the reviews of Nolen and Schiffer [10], an underestimation of the CDE of about 7% remains unsolved. This effect is known

³The choice of which value of the isospin projection represent neutrons and which protons is arbitrary, for example it could have been chosen to assign $T_z = 1/2$ for the proton and $T_z = -1/2$ for the neutron.

as the ‘‘Nolen-Schiffer’’ anomaly [10]. Studying mirror nuclei, and nuclei belonging to multiplets with $T \geq 1$, make possible to give an estimation of which is the nature of isospin breaking effects, and in particular if they can also be originated by the strong nuclear interaction. We can define the CDE between the lowest energy multiplets as [11]

$$CDE(T, T_z) = M_{T, T_z} - M_{T, T_z+k} + k\Delta_{nH}, \quad (1.7)$$

where T_z is the isospin projection of the nucleus with larger- Z , M_{T, T_z} its mass, M_{T, T_z+k} the mass of the nucleus after having substituted k protons with neutrons, and Δ_{nH} is the neutron-Hydrogen mass difference. Equation (1.7) can be rewritten in terms of binding energies. It has been shown by Wigner [12] in its famous *isobaric multiplet mass equation* (IMME), that the binding energy of a nucleus can be expressed in function of T_z as

$$\Delta BE(\alpha TT_z) = a + bT_z + cT_z^2 \quad (1.8)$$

where the coefficients a , b and c depends only on T and they are proportional to the isoscalar, isovector and isotensor component of the reduced matrix elements respectively. This equation remains valid in the presence for any type of isospin non-conserving interaction, because only the coefficients would be affected by the presence of such effects. Substituting equation (1.8) in equation (1.7) the CDE for two adjacent members of a multiplet becomes

$$CDE(T, T_z) = -b - c(2T_z - 1) + \Delta_{nH}. \quad (1.9)$$

If we extend also to excited multiplets states the difference in excitation energy are more generally called Coulomb Energy Differences (CED), in particular, if we refer to a pair of mirror nuclei they are called mirror energy differences (MED),

$$MED_{J,T} = E_{J,T,T_z(Z_>)}^x - E_{J,T,T_z(Z_<)}^x \quad (1.10)$$

where J is the total angular momentum, and $Z_>$ ($Z_<$) refers to the component with larger(smaller) Z . If we consider an isobaric triplet, $T = 1$, one can also define the triplet energy differences (TED) as

$$TED_{J,T} = E_{J,T,T_z=-1}^x + E_{J,T,T_z=+1}^x - 2E_{J,T,T_z=0}^x. \quad (1.11)$$

MED and TED can also be expressed in function of the coefficients of the IMME. Substituting equations (1.10) and (1.11) in (1.8), we found that $MED_J \propto \Delta b_J$ and $TED_J \propto \Delta c_J$, where b_J and c_J represent the variation in the b and c coefficients as function of the spin relative to the ground states.

So the MED is directly proportional to the isovector term in the IMME, while the TED to the isotensor one. The first give us information about the charge-symmetry of the nuclear interaction, while the second about the charge-independence. It is worth stressing that in these calculations ground state binding energies are normalized to zero, so the effect of the Coulomb interaction almost cancels out. Obtaining information about these terms, MED and TED, can give an estimation on the degree of isospin symmetry violation on the strong nuclear force.

Moving out of stability we can expect that symmetry violating terms became more important and easier to highlight. In particular nuclei populated in the experiment analyzed in this work, such as ^{56}Zn ($T_z = -2$), ^{55}Cu ($T_z = -3/2$) and ^{56}Cu ($T_z = -1$) are of particular interest because few or no information are available about MED or TED from them at present.

Chapter 2

Experimental Setup

The study of the isospin symmetry in nuclei implies the experimental investigation of mirror pairs and isospin analogue multiplets. Most often, while one of the nuclei in the comparison lie in the stability valley, the other is a radioactive nucleus. These nuclei are often characterized by low production cross section and very short half-lives, and require sophisticated experimental techniques in order to study them. The considerable improvements over the past decades in the field of heavy ion accelerator [13], ion sources, in-flight and on-line production and separation of unstable nuclear isotopes have made possible to extend studies to nuclei far from stability. Radioactive Ion Beams (RIBs) facilities nowadays can be found all over the world, examples are RIKEN Nishina Center (Japan), NSCL (Michigan, US), GANIL (France), ISOLDE (CERN, Switzerland), TRIUMF (Canada) [14, 15, 16]. Among them RIKEN-Nishina Center, GANIL, and NSCL use the in-flight separation technique, while ISOLDE and TRIUMF are examples of facilities using the on-line procedure. The differences between these two methods of producing and separating isotopes can be understood looking at Figure 2.1. The on-line separation technique historically was the first developed. The source impinge on a target sufficiently thick to stop the recoil reaction products that are then transported into an ion source and separated through chemical selection and then electromagnetic selection. A high-purity and low-energy beam is thus produced. The beam, then, can be post-accelerated to reach the desired energy. In the in-flight separation technique instead, the intermediate energy beam ($E > 80$ MeV) impinge onto a target, and then the reaction product or fragments can be directly collected using a momentum selecting separator. This technique needs no reacceleration, but the momentum spread of the beam might be important.

The experiment here reported, was performed at the Radioactive Ion Beam Factory (RIBF) that offers the highest beam luminosity available in

the world nowadays, and therefore at the moment is the only place where such exotic isotopes can be produced.

In our experiment a source of ^{78}Kr was used, the energy and the intensity of the beam were, on average, 345 MeV/u and 300 pA. To reach these val-

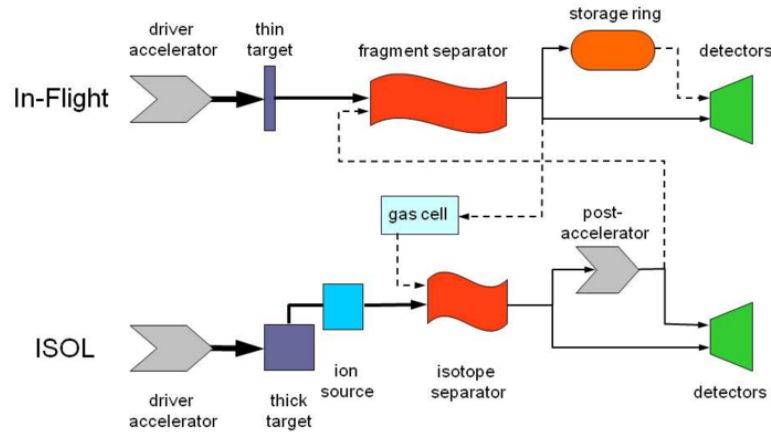


Figure 2.1: Schematic representation of the two different techniques for producing and separating RIBs. On top the Isotope Separation On Line (ISOL) technique, while on bottom the in-flight method.

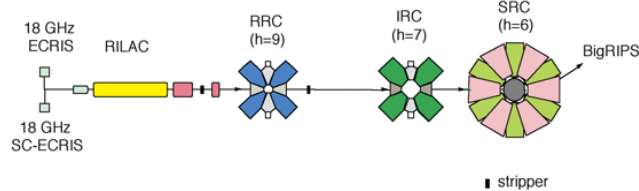


Figure 2.2: Schematic representation of the RIBF heavy-ion accelerating system, image taken from [17].

ues at the RI Beam Factory (RIBF), the acceleration mode for medium-mass ions, such as Calcium and Krypton, was used. The beam is accelerated passing through the RILAC (RIKEN Heavy-ion Linac), the K540 ring cyclotron (RRC), the intermediate step ring cyclotron (IRC), and the superconducting ring cyclotron (SRC) as schematically shown in Figure 2.5. In Figure 2.3 a schematic representation of the RIBF facility is reported. Once the Kr-nuclei leave the SRC, they are fragmented into the lighter isotopes on a 7-mm thick ^9Be primary target at the entrance of the BigRIPS separator.

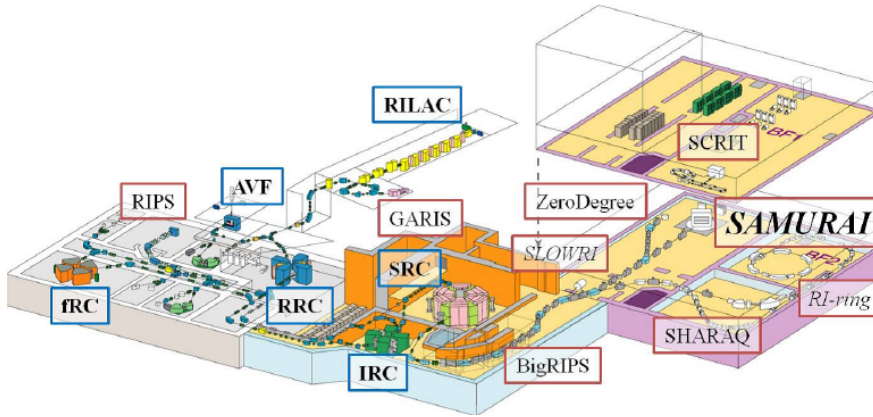


Figure 2.3: Schematic representation of the RIBF (Radioactive Ion Beam Factory) at RIKEN, Japan. Image taken from [18]

This secondary beam is then composed by the nuclei we want to study. A schematic view of the projectile fragmentation is shown in Figure 2.4. This process can be described in two steps called abrasion-ablation stages [19]. The model assumes is that the projectile and target make clean cylindrical cuts through each other [20], leaving, in our case, a spectator piece of the projectile which, during the ablation phase, emits light particles and γ -rays becoming the "fragment" observed. In our case the nucleus we wanted to be mostly populated was ^{57}Zn in the secondary beam, in order to produce ^{56}Zn after the interaction of ^{57}Zn with the second Beryllium target placed through the beamline. In this specific case the isotope separation *in-flight* technique is used [13, 21] to select these two nuclei in their respective beams and this will be described in details in the next Sections. In Section 2.4 instead, after having introduced the experimental setup used for particle separation and identification, the detectors array used for the γ analysis will be presented.

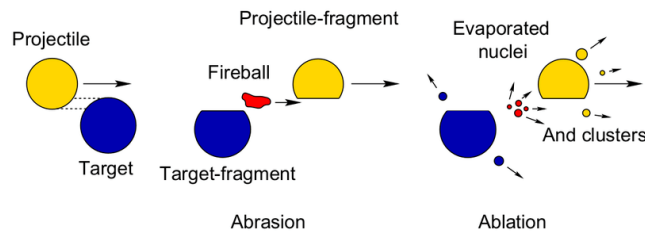


Figure 2.4: Schematic view of the projectile fragmentation according to the abrasion-ablation model.

Table 2.1: Some of BigRIPS separator parameters [22].

$\Delta\theta[mr]$	± 40
$\Delta\phi[mr]$	± 50
$\delta[\%]$	± 3
$P/\Delta P$ (1st stage)	1260
$P/\Delta P$ (2nd stage)	3420
Max. $B\rho[Tm]^*$	9.5/8.8
Lenght [m]	78.2

*9.5 is relative to the first stage, while 8.8 to the second one.

2.1 The BigRIPS separator

For this experiment, we want maximize the production of the ^{57}Zn isotope. For this purpose the BigRIPS separator was used.

The BigRIPS separator is divided into two stages as reported in Figure 2.5. The first stage is composed by four superconducting quadrupole triplets (STQ1-STQ4), and by two room-temperature dipoles with a bending angle of 30 degrees (D1 and D2) [22]. The second stage is made by four dipoles (D3-D6) and eight STQs (STQ7-STQ14). Along the separator we find several focal planes (F1-F7) and a wedge-shaped degrader is placed in F1 focus. The large acceptance of BigRIPS makes possible to expand the accessible region of exotic nuclei. In Table 2.1 are reported its basic parameters, with $\Delta\theta$ and $\Delta\phi$ indicating the vertical and horizontal acceptances, while δ is the momentum acceptance. The separation of the first reaction products is done thanks to the fact that nuclei with different mass-to-charge ratio are deflected differently and, consequently, follow different trajectories. The magnetic rigidity of a particle is defined as

$$B\rho = \frac{p}{q} = \gamma \frac{Au}{Ze} \beta c, \quad (2.1)$$

where p and q represents the momentum and charge of the particle respectively and $\gamma = 1/\sqrt{1-\beta^2}$, $u = 931.5 \text{ MeVc}^2$ is the atomic mass unit, e the electron charge and the product Au is the mass of the nucleus. From equation (2.1) it is clear that the curvature radius ρ is directly dependent on the ratio A/Q , where $Q=Ze$. For this reason nuclei with a different mass-to-charge ratio will be focused in different place after the dipoles. After two dipole stages, the particles are refocused to a single point in the focal plane, independently on their A/Q . This is the operating principle of an

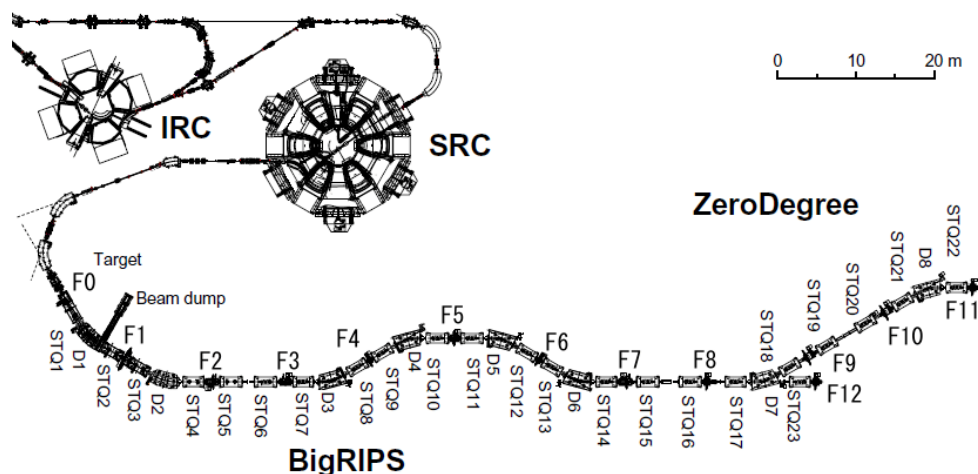


Figure 2.5: Schematic of the BigRIPS separator shown along with the IRC and SRC cyclotrons and of the ZeroDegree spectrometer. Image taken from [23]

achromatic separator. Particle separation is not possible using only dipoles and quadrupoles since the same A/Q can be obtained by different combinations of A and Z [24]. Isotope identification can be accomplished inserting wedge-shaped degrader in the focal planes F1. The shape of the degrader can be chosen in such a way that the achromaticity is preserved after passing through it. It is exactly the achromaticity condition that determines the wedge angle. When passing through the degrader the particles lose energy in matter according to the Bethe-Bloch formula

$$\frac{dE}{dx} = -\frac{4\pi e^2 Z^2}{m_e v^2} N_m Z_m \left[\ln\left(\frac{2m_e v^2}{I}\right) - \ln\left(1 - \frac{v^2}{c^2}\right) - \frac{v^2}{c^2} \right], \quad (2.2)$$

where m_e is the electron rest mass, I the average ionization potential of the material and N_m and Z_m the number density and the atomic number of the target [25]. Isotopes with different Z will lose a different amount of energy passing through the degraders, and will exit with different velocities, that, for nuclei with the same A/Q , means different rigidities, and different trajectories. By this way it is possible to select the species and the isotopes of interest and to transport them to the reaction target where the secondary reaction takes place. The products of this secondary reaction need to be identified as well and this task will be accomplished by a recoil spectrometer which name is ZeroDegree.

2.2 The ZeroDegree spectrometer

The ZeroDegree spectrometer, Figure 2.5, consists in two dipoles (D7-D8) and six STQs (STQ17-STQ22), with focal planes F9 to F11. There is an intermediate region, used as a matching section, between BigRIPS and ZeroDegree, where the secondary target is placed, it is composed by the foci F7 and F8 and by the STQ15 and STQ16.

2.3 Particle identification

The particle identification, which consists in the measurement of A/Q and Z , in BigRIPS and ZeroDegree is accomplished with the TOF- $B\rho - \Delta E$ method. In the equations (2.1) and (2.2) we can see that A/Q and the energy loss in the matter depends on the velocity $c\beta$ of the particle. For this reason, a measurement of the time-of-flight is needed. The time-of-flight between two points is defined as

$$TOF = \frac{L}{\beta c} \quad (2.3)$$

$$\frac{A}{Q} = \frac{B\rho}{\gamma u} \frac{1}{\beta c} \quad (2.4)$$

$$Z = K_1 \beta \sqrt{\frac{\Delta E}{\ln(2m_e c^2 \beta^2 / I) - \ln(1 - \beta^2) - \beta^2}} + K_2, \quad (2.5)$$

where L is the flight path length. The other two equations, one for the atomic number Z and the other for the mass-to-charge ratio A/Q , were retrieved making use of the equations (2.1), (2.2). In the last equation, in particular, K_1 and K_2 represent calibration parameters to be determined experimentally, see Chapter 4. This three equations together represent the information we want to obtain for each event during the experiment, this is in brief the TOF- $B\rho - \Delta E$. In the following paragraphs the general techniques and the detectors used during this experiment are presented.

2.3.1 The $B\rho$ measurement

$B\rho$ measurement is performed by trajectory reconstruction and velocity determination. This is possible using Parallel Plate Avalanche Counters (PPACs) in F3, F5 and F7 for BigRIPS, and in F8, F9 and F11 for ZeroDegree (see 2.3.2), with which we can measure positions and angles of fragments and with ion-optical transfer matrix, deduced from experimental data, it is

possible to reconstruct the trajectory. The absolute $B\rho$ value of the fragments is determined measuring the dipoles magnetic field with NMR probes and the central trajectory radii of the magnets [26].

2.3.2 The position measurement

As previously mentioned, the position measurement is made using PPACs, Figure 2.6. PPAC detectors have a sensitive area of $240\text{ mm} \times 150\text{ mm}$, and

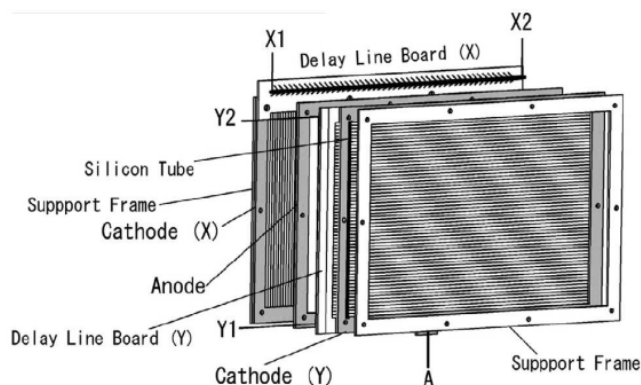


Figure 2.6: Schematic representation of a delay-line PPAC, image taken from [27].

the position information is obtained by a delay-line readout method [27]. They are called double-PPAC when they are used in couple, in order to reach high detection efficiency. Each PPAC measure the position of the incident particle in two dimensions. The detector consists in two thin electrode separated by 3-4 mm and filled with gases such as isobutene (C_4H_{10}) and perfluoropropane (C_3F_8). When an incident particle passes through the PPAC, it creates ionized electrons and if a voltage is applied between the anode and cathode, this causes an *electron avalanche*. In this process, as it is schematically represented in Figure 2.7, electrons, accelerated by a potential difference, collide with other atoms in the medium and ionize them, releasing additional electrons which accelerate and collide themselves [25]. Because the electrons move at high mobile velocity, these detectors have good time response. As we can see from Figure 2.6, from each PPAC we collect five signals that we pass through a TDC to obtain finally: T_{X1} , T_{X2} , T_{Y1} , T_{Y2} and T_A . From these we can find the impact point of the incident particle,

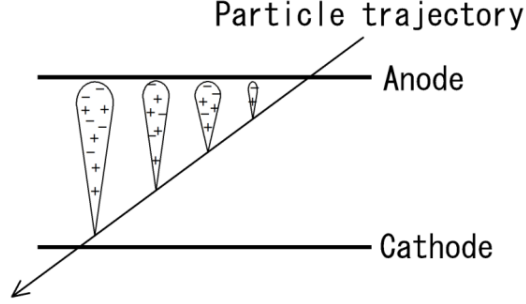


Figure 2.7: Electron avalanche caused by an incident ionizing particle, image taken from [27].

simply using the following equatons

$$x = k_x \frac{T_{x1} - T_{x2}}{2} + X_{offset} \quad (2.6)$$

$$y = k_y \frac{T_{y1} - T_{y2}}{2} + Y_{offset} \quad (2.7)$$

where k_x and k_y (mm/ns) are the position coefficient, and X_{offset} and Y_{offset} (mm) are the offset correction. The quantities T_{sumX} and T_{sumY} defined as

$$T_{sumX} = T_{X1} + T_{X2} - 2T_A \quad T_{sumY} = T_{Y1} + T_{Y2} - 2T_A, \quad (2.8)$$

are constant for each PPAC and independent from the impact position of the particle. Only events with valid T_{sumX} and T_{sumY} will be considered during data analysis. From double-PPAC we can extract four measurement of x and y . Finally performing a linear track reconstruction, we can obtain the particle trajectory.

2.3.3 The TOF measurement

The time-of-flight measurement of nuclei is obtained using plastic scintillators placed in F3 and F7 for BigRIPS and F9 and F11 for ZeroDegree. From equation (2.3) the time-of-flight in BigRIPS become,

$$TOF = \frac{L_{37}}{\beta_{37}c}, \quad (2.9)$$

while in ZeroDegree it is

$$TOF = \frac{L_{811}}{\beta_{811}c}. \quad (2.10)$$

Each scintillator is connected to a PMT at each side and the charge collected by the PMTs is related to the position as

$$q_1 = q_0 \exp\left(-\frac{L+x}{\lambda}\right) \quad q_2 = q_0 \exp\left(-\frac{L-x}{\lambda}\right), \quad (2.11)$$

where q_1 and q_2 represent the charge accumulated at each side of the scintillator, λ is the attenuation length of the light in the scintillator material, $2L$ is the length of the scintillator, q_0 the total charge accumulated and x the horizontal impact point of the incident particle [26]. Inverting the equations (2.11), is possible to obtain position information as

$$x = \frac{\lambda}{2} \ln\left(\frac{q_1}{q_2}\right). \quad (2.12)$$

This can be related also to the time information obtained from the scintillator, knowing that

$$x = \frac{V}{2}(t_2 - t_1), \quad (2.13)$$

here t_2 and t_1 represent the time measured from left and right PMTs. From equations (2.13) and (2.12) we obtain a time-to-charge correlation

$$\lambda \ln\left(\frac{q_1}{q_2}\right) = V(t_2 - t_1). \quad (2.14)$$

To remove the position dependencies in the time-of-flight, the time measured by the plastic scintillators is defined as

$$t(Fx) = \frac{1}{2}(t_1 + t_2), \quad (2.15)$$

where Fx denotes the focus in which the detector is placed [28]. Then, the time-of-flight is simply obtained as

$$TOF_{37} = t(F7) - t(F3) + t_{offset}(37) \quad (2.16)$$

$$TOF_{811} = t(F8) - t(F11) + t_{offset}(811) \quad (2.17)$$

here the time offset has to be determined experimentally.

2.3.4 The ΔE measurement

In order to determine the atomic number of the incident nucleus a ΔE measurement is performed using a Tilted Electrode Gas Ionization Chamber (TEGIC) [29, 30]. It consists in thirteen cathode and twelve anode

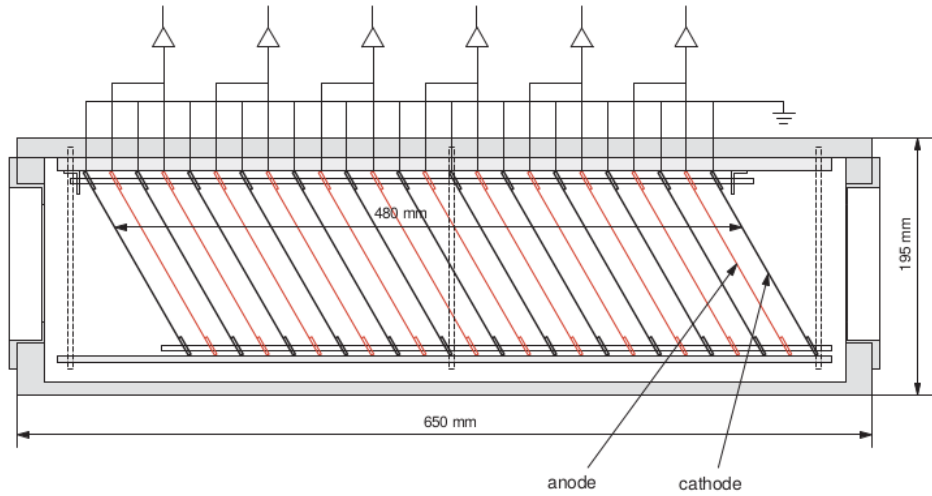


Figure 2.8: Cross-sectional view of the gas ionization chamber used in the experiment, image taken from [29].

planes, made of thin conductive foils, alternately placed in 20-mm steps as in Figure 2.8. They are tilted 30° toward the center to avoid the recombination of electrons and positive ions created by the incident particle when passing through the detector. These electrodes are then enclosed in an aluminium chamber, equipped with Kapton windows of $50\text{-}\mu\text{m}$ thickness. To reduce the number of electrical outputs, pairs of anode electrodes are connected together, resulting in six anode outputs. Also the cathode electrodes are connected together and grounded. When electrons and positive ions move towards the respectively electrodes, the anode potential drops, until it reaches the value equal to the sum of electrons and ions charges liberated by the traversing particle, and this is proportional to the energy loss ΔE . One TEGIC is placed after F7 focus in BigRIPS, and another after F11 in ZeroDegree. Then Z is obtained from the equation (2.5) after having find the optimum value of the calibration parameters K_1 and K_2 .

2.4 The DALI2+ array

DALI2+ consists in a $^{226}\text{NaI(Tl)}$ detector array employed for γ -rays detection [31]. The scintillator crystals are then coupled to PMTs. In Figure 2.9 it is reported a representation of the array. As we can see, the crystals are arranged to form different layers perpendicular to the beam axis. The setup is optimized to cover the largest possible range of angles, that in this case

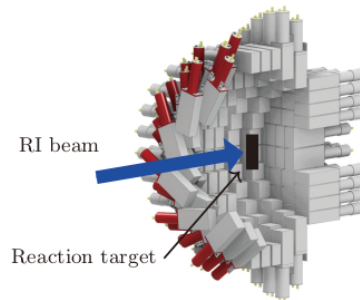


Figure 2.9: Schematic 3D representation of DALI2+ array. Images taken from [31].

Table 2.2: GEANT4 simulated FEP efficiencies and energy resolution of DALI2+ for $v/c=0.6$. *Efficiencies and resolution with 15 cm radius add-back.

E_γ (MeV)	eff. (%)	FWHM (keV)	eff. (%)*	FWHM (keV)*
0.5	40	38	48	43
1.0	24	76	34	85
2.0	15	139	23	155

is from 18° to 122° in the laboratory frame [32]. Typical Full-Energy-Peak efficiencies (FEP) and energy resolutions are listed in Table 2.2 for different values of E_γ [31]

In addition, due to the Lorentz boost the angular distribution of the emitted radiation is forward peaked in the laboratory frame, so it is important to cover the smallest possible angles [33]. The array surround a vacuum pipe, in which the secondary target is placed. In this experiment it consists in a 6-mm thick ^9Be -target. The secondary beam, after passing through BigRIPS, hits the target and produces ejectiles populating excited states. In decaying to the ground state, the nuclei emit γ -rays that are shifted in energy as a consequence of the Doppler Effect. The granularity of the array allows the reconstruction of the direction of each gamma-ray. The Doppler correction provides the energy of the transition in the reference frame of the nucleus.

Chapter 3

Data analysis

The exotic beams produced with fragmentation of intermediate energy beams are generally of very low intensity and contaminated by neighbouring nuclei. It is of fundamental importance to obtain an event-by-event identification of the reaction products. This is performed using a variety of detectors that needs proper data selection and calibration and this work will be described in this Chapter.

In the first section the efficiencies of the BigRIPS and ZeroDegree PPACs are presented, then the temporal behaviour of the other detectors is checked in order to ensure the correct operating of the apparatus.

As mentioned at the beginning of this work, this experiment was concerned on the analysis of one-neutron knockout reactions from proton-rich nuclei. The setting was chosen to be centered on ^{57}Zn isotope in BigRIPS and on ^{56}Zn isotope in ZeroDegree and this made possible to study also other exotic nuclei like ^{56}Cu and ^{55}Cu .

3.0.1 Triggers

The first step of data selection takes place online during data taking thanks to the use of different triggers. When a particle passes through BigRIPS, to be registered as a valid event a signal has to be obtained in the F7 plastic that is located in the final part of the separator see Figure 2.5. The same can be said for ZeroDegree with F11 plastic located at the end of the beamline see Figure 2.5. The type of event is identified by a number that is called *fbt* and its value is decided by the coincidence module. During the experiment the DAQ was triggered by the following two physical triggers:

- F7(DS): F7 plastic down-scale with a scaling factor of 15 is used for BigRIPS. The scaling factor is necessary because of the large intensity

Table 3.1: Possible triggers and coincidence registers fbit values combinations.

Trigger	fbit
F7(DS) (phys)	1
F7xF11	2
F7(DS) and F7xF11	3
F7xF11xDALI2 (phys)	4
F7(DS) and F7xF11xDALI2	5
F7xF11 and F7xF11xDALI2	6
F7(DS) and F7xF11 and F7xF11xDALI2	7

of particles reaching F7. This trigger means that a particle has reached F7 plastic. Only one every fifteen particles that trigger the DAQ will be registered as F7(DS) events.

- F7xF11xDALI2: this is the second physical trigger and it means that an incident particles after reaching F7 focus, has hit the secondary target, emitted γ -rays seen by DALI2 and has finally reached the F11 plastic.

There are also coincidence registers that are not triggers, but at which an fbit value is assigned. All the possible combinations of fbit values of triggers and coincidence register are listed in Table 3.1. The starting points are fbit values equal to 1, 2 and 4 from which combinations all the other values can be created.

Only combinations in which at least one fbit value associated to a physical trigger is present will be registered, this means that events with associated fbit value equal to 2 are not selected by the trigger. Events with an fbit value equal to 3 arise from the simultaneously fulfilment of fbit equal 1 and 2 conditions. The F7xF11xDALI2 trigger, which means that the particle has reached F7-plastic, reacted in the target emitting gammas and finally reached F11-plastic, automatically fulfill also the F7xF11 one, because the latter is a less stronger condition and does not request the observation of gamma-rays. Events are not labelled with an fbit number equal to 4 because they automatically fulfill the fbit equal to 6 condition. Same argument can be applied for events which simultaneously trigger F7(DS) and F7xF11xDALI2 (fbit=5). These events satisfy the conditions for fbit equal to 7 and as such they are recorded. The valid triggers remain 1, 3, 6 and 7.

3.1 BigRIPS and ZeroDegree

3.1.1 PPAC and Focal Plane efficiencies

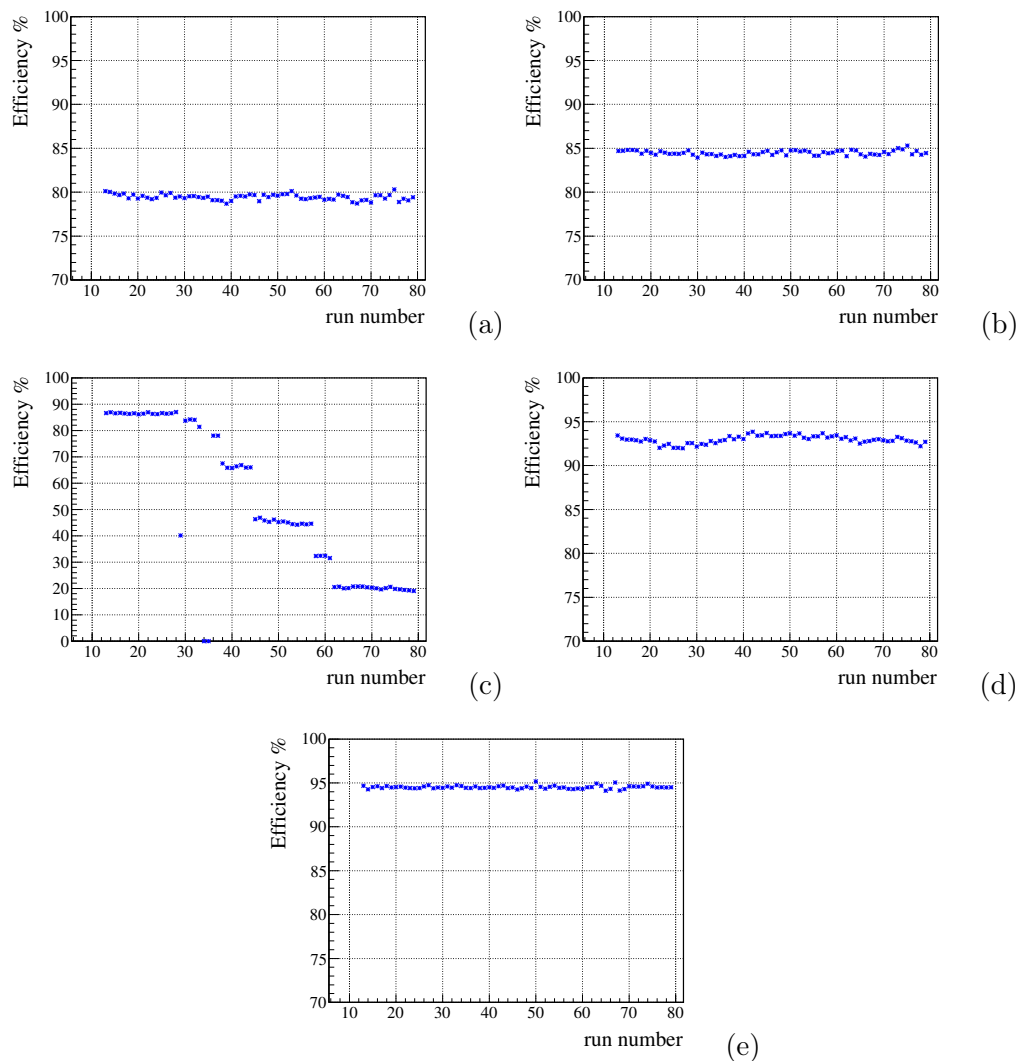


Figure 3.1: Example of PPACs efficiencies: (a) PPAC 3-1A, (b) PPAC 5-1B, (c) PPAC 7-1B, (d) PPAC 9-2B and (e) PPAC 11-2A.

The accuracy of the position reconstruction is the first step. To do this, it is necessary to evaluate the correct operating of PPACs. As pointed out in Section 2.3.2 of Chapter 2, only events that have a valid T_{sumX} and T_{sumY} are considered. From each PPAC one x and one y position information can

be obtained, so using two double-PPAC provide four position information for the x position and four also for the y . In principle this data are redundant to reconstruct the trajectories of the incident particles and we only need that at least two PPACs for each Focal Plane are working. To monitor their operating their efficiency has to be checked. The efficiency is defined as

$$\epsilon_{PPAC} = \frac{N_{PPAC}}{N_{plastic}}, \quad (3.1)$$

where N_{PPAC} is the number of valid events that are registered by each PPACs, while $N_{plastic}$ is the number of events seen by the plastic scintillator. The normalization factor is taken from the plastic detectors because they are the fastest and most efficient ones. In Figure 3.1 some examples of these efficiencies are reported as a function of the acquisition run number¹. From panel (c) it is clear that there were some issues with PPAC 7-1B during the experiment. This did not affect significantly the trajectory reconstruction, as we will explain later.

It is possible to define the focal planes efficiencies as

$$\epsilon_{fpl} = \frac{N_{fpl}}{N_{plastic}}, \quad (3.2)$$

where N_{fpl} is the number of valid events reconstructed in the foci. In Figure 3.2, examples of F3, F5, F7, F9 and F11 efficiencies are showed. It is clear that these efficiencies are larger than the respective PPACs ones, this is because focal planes positions reconstruction can be performed with any number of "good" PPACs. For example if one plane of the double-PPAC has low efficiency, such as the F7-1B in our case, the focal plane position can still be reconstructed from the other three plates. The PPACs allows to define the positions and angles in focal planes, needed for trajectory reconstruction. The latter can be retrieved making a linear track reconstruction, or in other words, once obtained position information from the PPACs, the projection of those values on the focal plane provide the angle of the particle trajectory in the horizontal and vertical directions [28]. In Figure 3.1 and 3.2 it is shown that PPACs, and consequently Focal Planes efficiencies increase with the PPAC ID. This is because of the very high rate of incident particle on the F3 focus, that makes more difficult a proper reconstruction. In general the obtained focal planes efficiencies are satisfactory, which implies a good trajectory reconstruction.

¹ To each PPAC in the beamline an identification number (ID) was given, the first number means to which focal plane it belongs and the second number together with the letter specify which plate it is. For example PPAC 3-1A is the first plate of the PPAC at the F3 focus, PPAC 3-1B is the second plate of the same double-PPAC and so on.

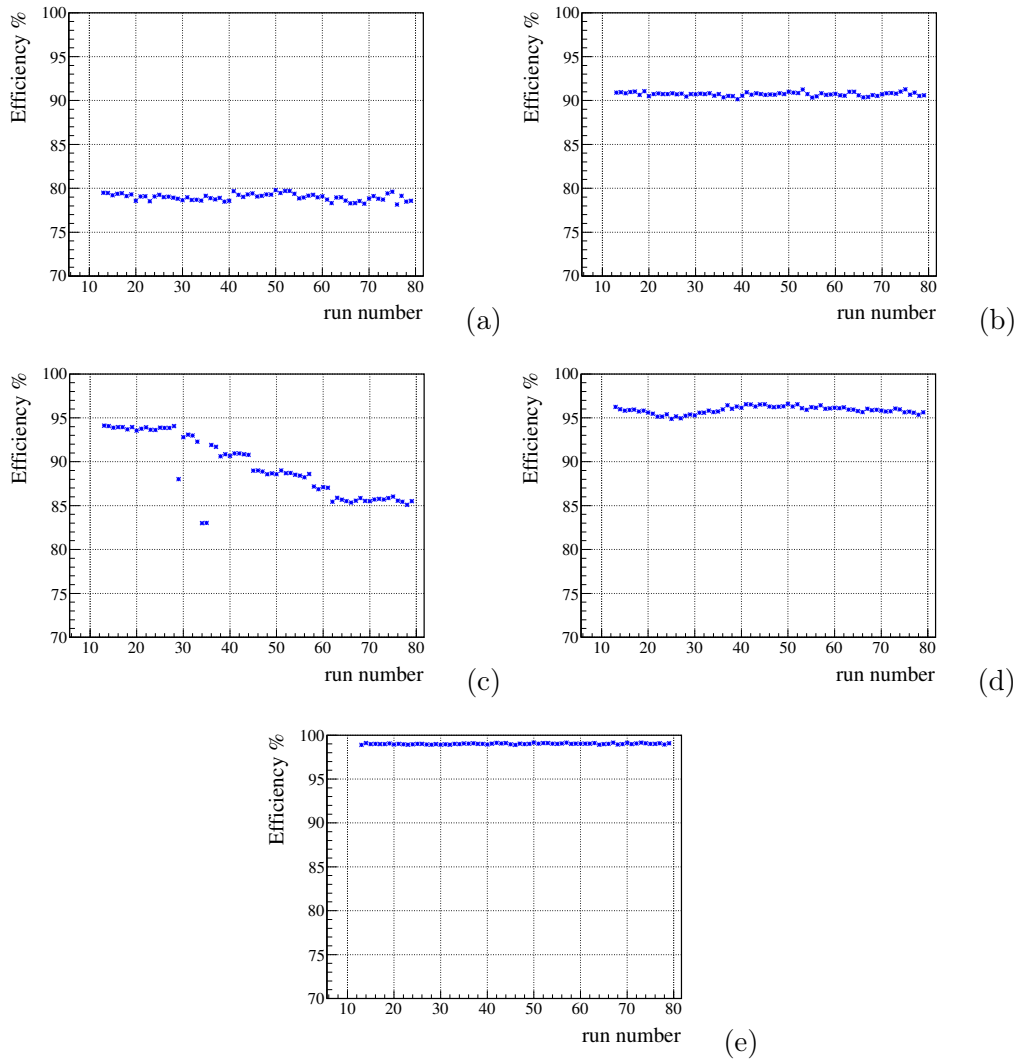


Figure 3.2: Example of focal planes efficiencies: (a) F3, (b) F5, (c) F7, (d) F9 and (e) F11.

3.1.2 Plastic detectors

The performance of the plastic detectors are analyzed with a study of the charge correlation was examined. The accumulated charge at the left PMT and the one accumulated on the right PMT are correlated. The bigger it is q_{left} , the smallest should be q_{right} because the charge accumulated depends on the impact position and their correlation spectrum should follow an exponential behaviour as expected from equations (2.11) and (2.12), where we should replace the labels 1 and 2 of the charge, with *left* and *right* to be consistent. In Figure 3.3 this correlation is reported for the four plastic placed

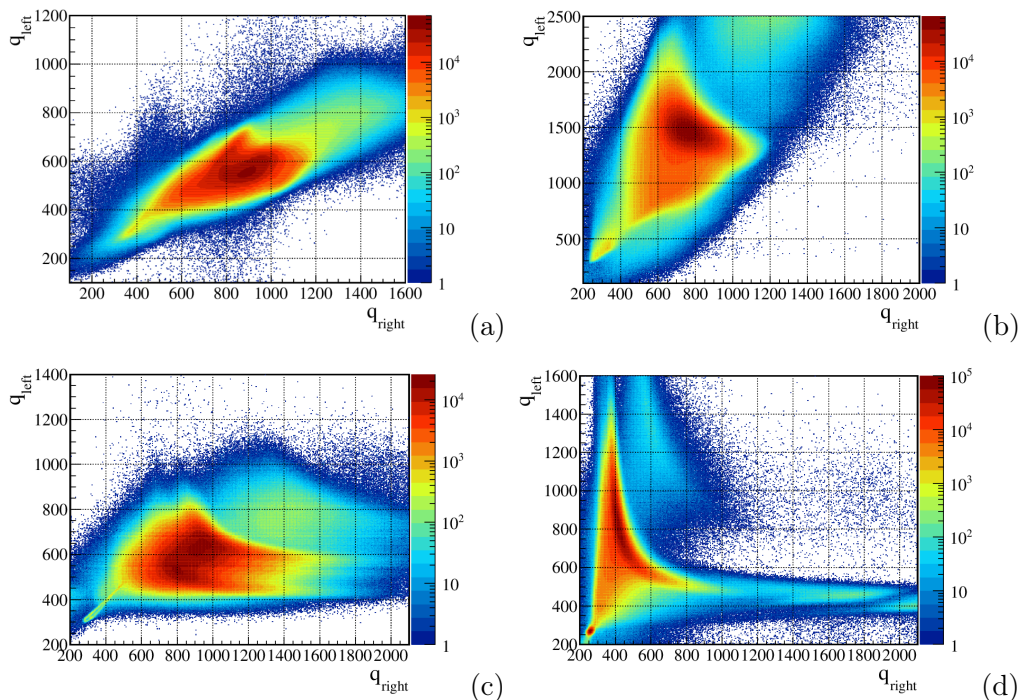


Figure 3.3: Charge correlation in plastic detectors placed in (a) F3, (b) F7, (c) F8 and (d) F11. Charge expressed in a.u.

in F3, F7, F8 and F11 and we can see that the distributions are the ones expected. It is also possible to notice a second structure in each plot, that becomes more evident in F11. This structure belongs to inconsistent events, such as multiple-hit events or δ -rays and it represents a background for the measurement [26]. Indeed, as mentioned in Chapter 2 PPAC detectors are filled with gases that can be ionized by an incident ion. The electrons such created can have enough energy to escape a significant distance away from

the primary radiation beam and produce further ionization. It can happen that bad events produce a trigger in F7-plastic which triggers the acquisition, but actually no charge was deposited on it, so for this event the pedestal will be integrated. Requesting correlation between detectors, such as that PPACs were actually fired, will make the spectrum cleaner. This request means that not only that we are reducing the time interval in T_{sumX} and T_{sumY} ² that we integrate to reconstruct events, but also that in this interval we are taking only good events. In Figure 3.5 (a) and (b), we see an example of the same spectra of Figure 3.3 but with the gate that F3 and F7 PPACs fired. This gate will remove also good events, because it requires that each plate of PPAC F3 and F7 has to be fired to make a consistent event. The statistics in these last plot is reduced to the 12% the one of those in Figure 3.3 (a) and (b). Another type of background comes from events where more than one particle hit the plastic, this can be removed using the Multi-hit-Time-to-Digital converter (MhTDC). When a valid event triggers the DAQ, all the events arriving in a certain time window are recorded. Rejecting high multiplicity events will remove this type of background.

Data sorting is further performed by the selection of properly time correlated events. From equation (2.13) we expect a linear dependence of the time measured at the left PMT upon the time measured at the right PMT, see Figure 3.4. Even for the time, the same arguments can be employed about inconsistent events as for the case of the charge. In Figure 3.5 (c) and (d) the same plots as Figure 3.4 (a) and (b). Then validity of equation 2.14 is verified and the results are plotted in Figure 3.6. A clear correlation can be seen, but background events are also present. The linear correlation can be better emphasized looking at Figure 3.5 panel (e) and (f) where the request that each PPAC was fired has been applied. As a last check the time behaviour of the time-of-flight measured in BigRIPS and in ZeroDegree is observed as shown in Figure 3.7. The TOF remains constant during the experiment thus not requiring corrections during the analysis.

3.1.3 Ionization chambers

In this paragraph the analysis of the ionization chambers placed after F7 focus in BigRIPS and after F11 in ZeroDegree is presented. In Figure 3.8 the temporal behaviour of these detectors is shown. In (a) the gain of one of the anodes couple of the F7-TEGIC³ is plotted as a function of the run number,

² When a particle passes through a PPAC plates it will results into two time information. Good events will have a constant and value of T_{sumX} and T_{sumY} determined by the detector itself.

³ See Section 2.3.4 for details on the gas ionization chambers.

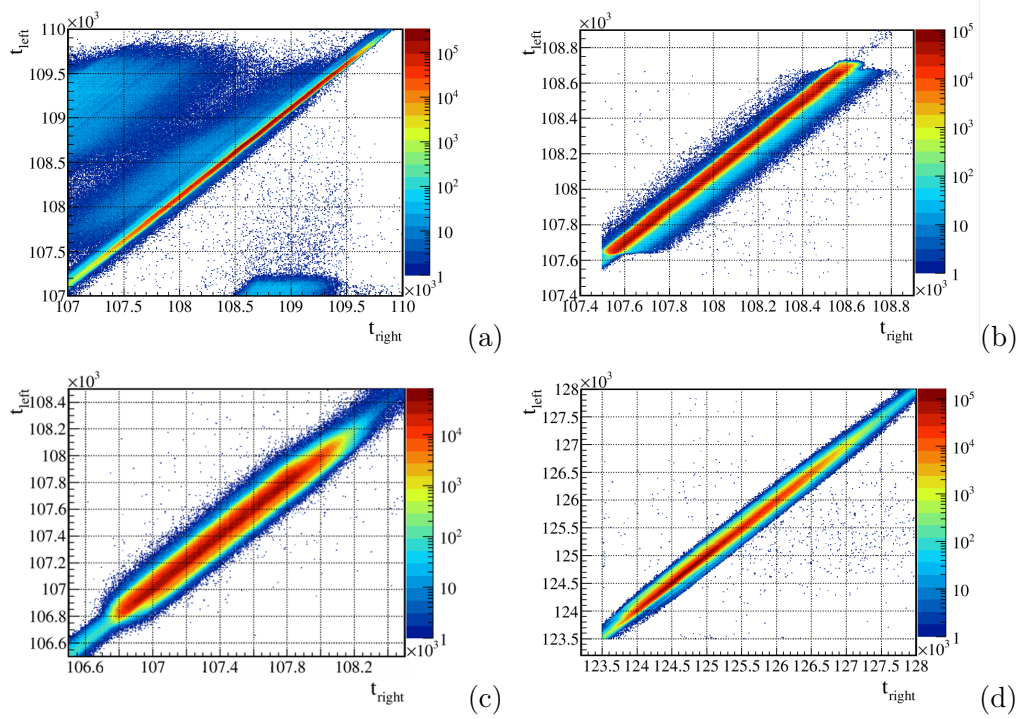


Figure 3.4: Time correlation in plastic detectors placed in (a) F3, (b) F7, (c) F8 and (d) F11. Time expressed in a.u.

3.1. BIGRIPS AND ZERODEGREE

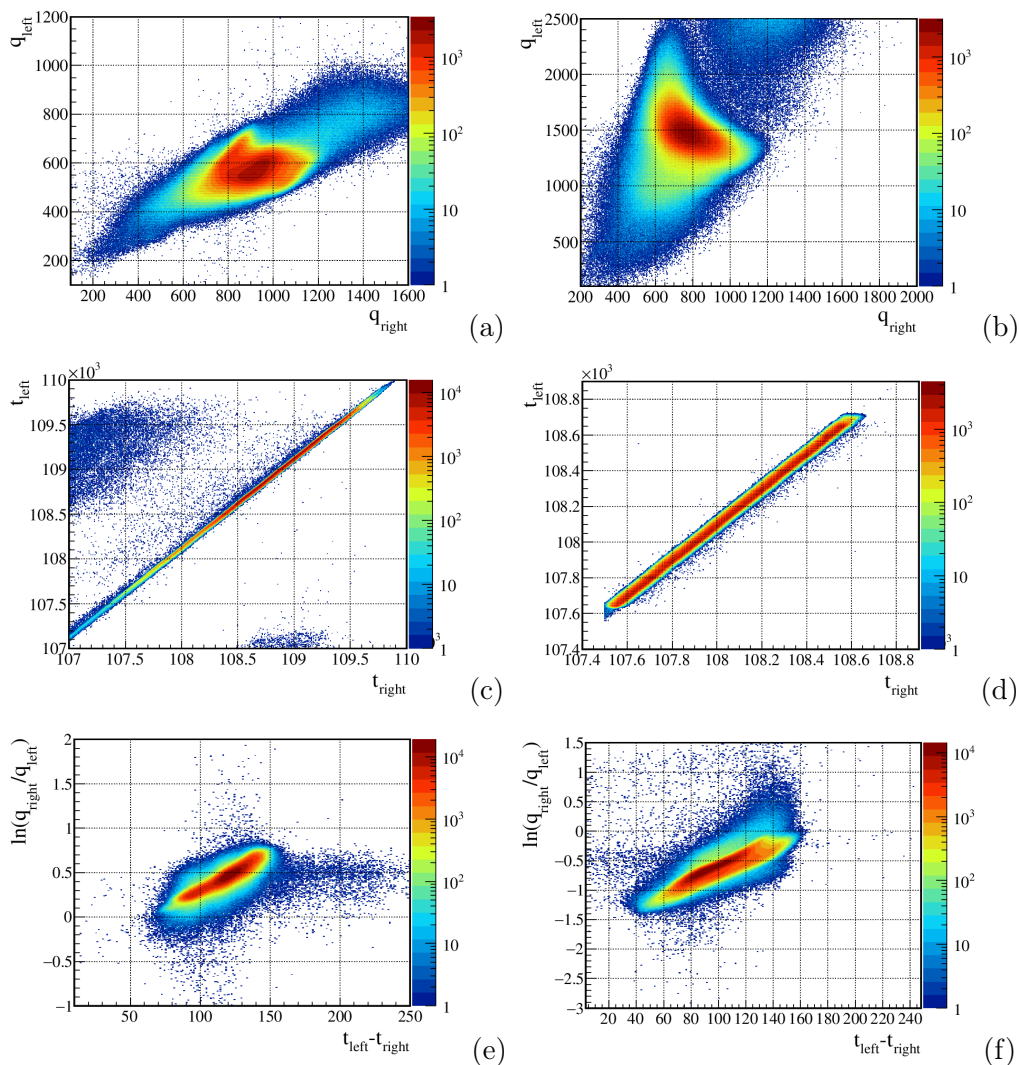


Figure 3.5: Charge and time correlation requesting that each PPAC was fired. Panel (a) shows charge correlation for the plastic detectors placed at F3 focus while panel (b) the same but for F7-plastic. Panel (c) and (d) instead report the time correlation for F3 and F7 plastic respectively. Finally panel (e) and (f) show the time-charge correlation for F3 and F7 plastic respectively.

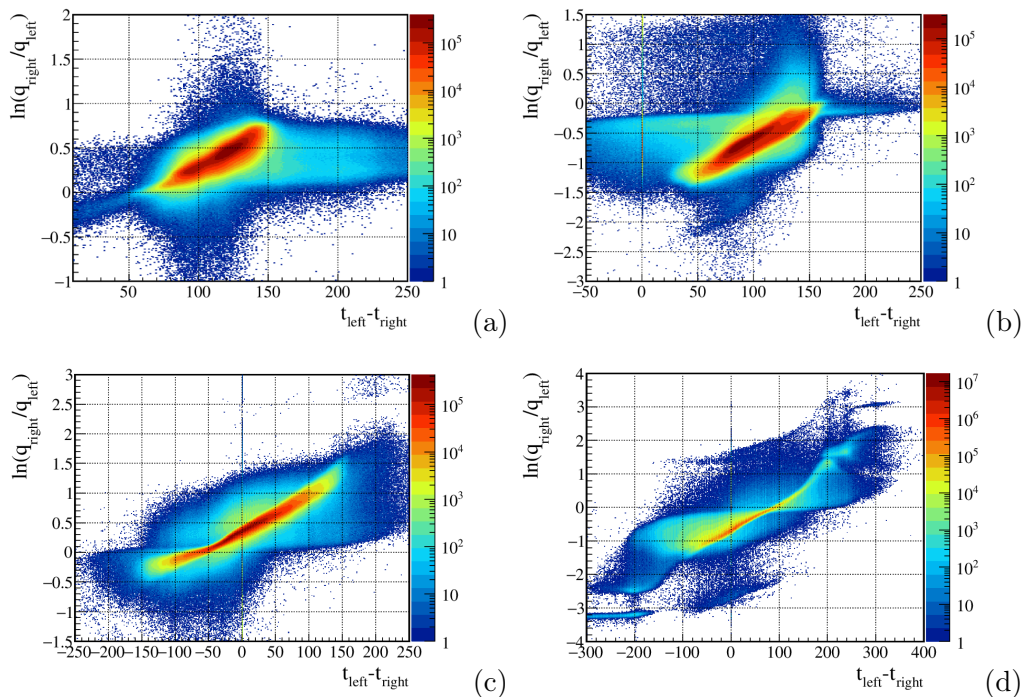


Figure 3.6: Time-to-charge correlation in (a) F3-plastic, (b) F7-plastic, (c) F8-plastic and (d) F11-plastic. On the y-axis is reported the logarithm of $q_{\text{right}}/q_{\text{left}}$ versus the difference between t_{left} and t_{right} on the x-axis. Charge and time expressed in a.u.

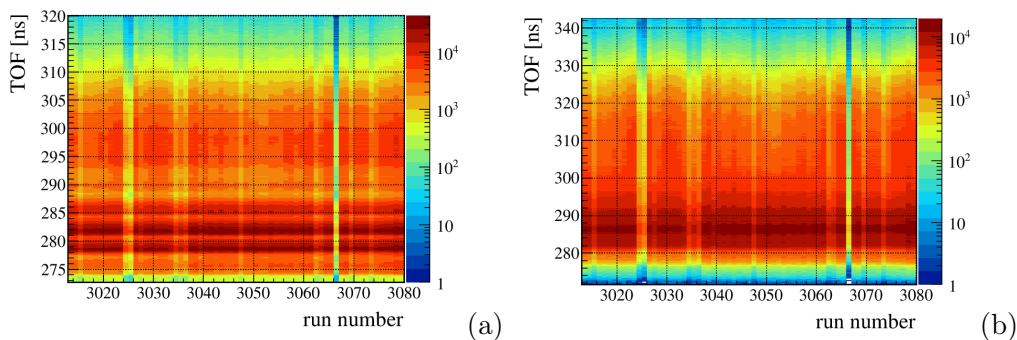


Figure 3.7: Temporal evolution of measured time-of-flight between (a) F3 and F7 plastic and (b) F8 and F11 plastic.

while in (b) the gain for the same anode couple is represented for F11-TEGIC. For this last detector, during the experiment, was observed a gain drift, so it was needed a gain match to compensate this effect. This occurs because the energy loss of a particle in the gas depends on its temperature and on its pressure, so small variation in these quantities will generate drifts in the amount of energy accumulated. The fact that we do not see gain drift in F7 means that these quantities remained constant over the experiment. This

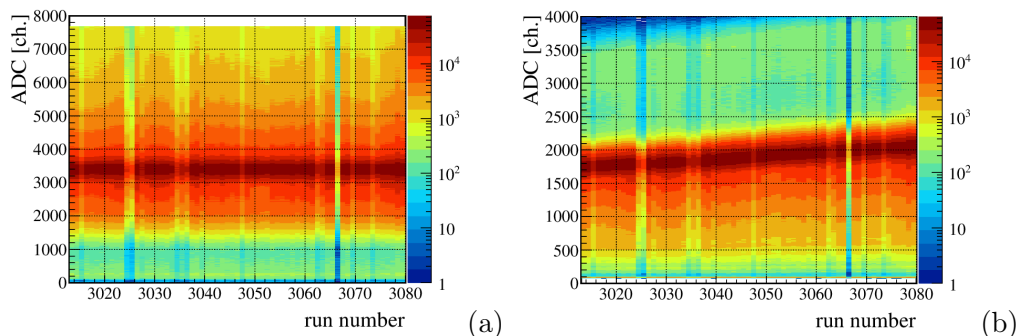


Figure 3.8: Examples of temporal behaviour of ionization chambers. (a) gain for the fourth couple of anodes in F7-TEGIC, (b) the same for F11-TEGIC, values expressed in a.u.

behaviour is reflected in the reconstructed atomic number in ZeroDegree. As we can see in Figure 3.9 (b) the Z values of the outgoing particles shifts during the experiment. In Figure 3.9 (c) this drift has been removed after having adjusted the F11-gain by shifting the centroids to a reference value.

3.2 The PID

Verified that the detectors in BigRIPS and ZeroDegree are consistent and properly calibrated, we can move to particle identifications. From the experimental setup it is possible to obtain particle identification (PID) from three different groups of parameters both in BigRIPS and in ZeroDegree. These are briefly called *rips*. For example, in BigRIPS, it is possible to obtain PID spectra with the time-of-flight measured between F3 and F7 (actually this is the only possibility), and position information and $B\rho$ values obtained from F3 and F5 (rips 3-to-5), F5 and F7 (rips 5-to-7) or F3 and F7 (rips 3-to-7). Because F7 is usually the most efficient focal plane, it is a convenient choice to use it. To avoid the high intensity of particles passing through F3, the most natural choice is the rips 5-to-7. In Figure 3.10 a

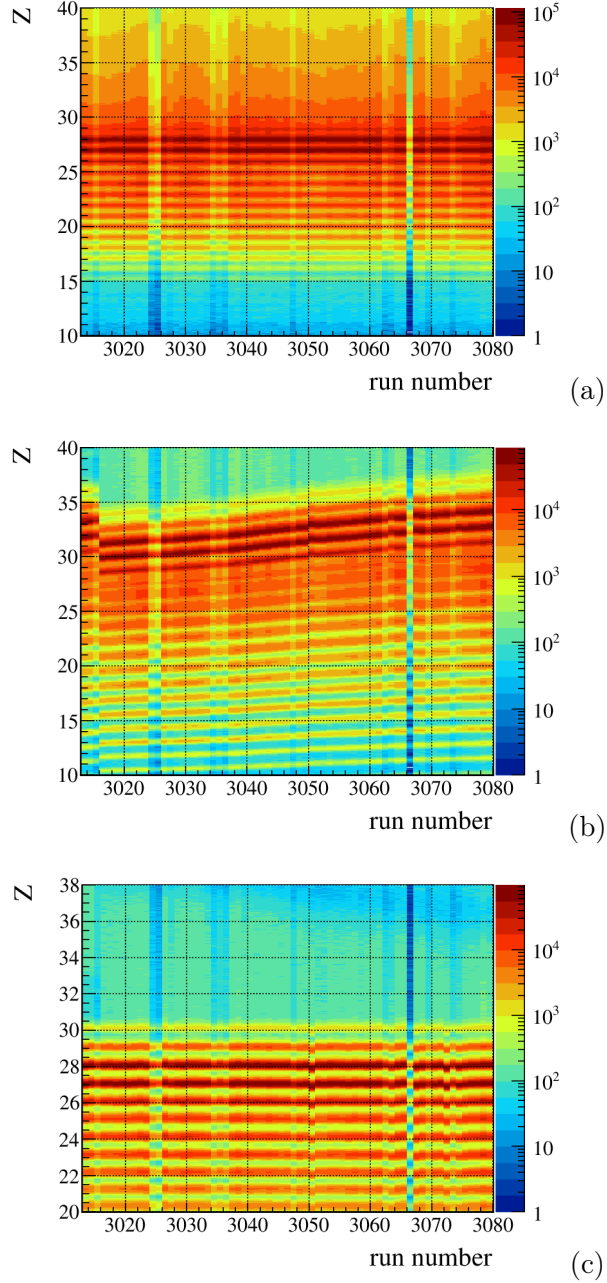


Figure 3.9: Reconstructed Z from ionization chambers. (a) Atomic number of incoming particles of secondary beam, obtained from F7-TEGIC, (b) Z value of particles outgoing after the interaction with the target in F8 focus, reconstructed from F11-TEGIC and (c) the same as (b) but with a drift correction implemented.

Table 3.2: Observed resolution and statistics from the three different BigRIPS rips for ^{56}Cu . In the first line the resolution is reported in percent, in the second line the respective statistics. These results have been obtained analysing only 50000 events of each acquisition runs.

	rips 3-5	rips 5-7	rips 3-7
res. (%)	0.16	0.24	0.16
stat.	10217	56861	66078

gaussian fit of the ^{56}Cu peak obtained from this last setting is shown, while in Table 3.2 the statistics and resolutions of incoming ^{57}Zn in BigRIPS are reported. Considering the lower efficiency of F3 focal plane respect to that of F5, the second rips was chosen. For ZeroDegree instead, the possibilities are: rips 8-to-9, 9-to-11 and 8-to-11. This time F11 is the most efficient focal plane and after checking resolutions and statistics, the better compromise was to choose rips 9-to-11.

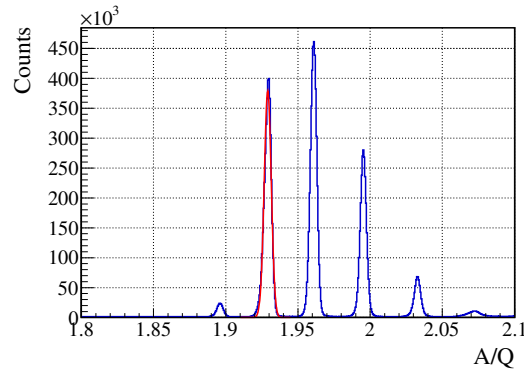


Figure 3.10: Projection of particle-identification spectrum on the Cu isotope. First peak at $A/Q=1.89$ is ^{55}Cu and the second at $A/Q=1.93$ is ^{56}Cu . Other peaks comes from the high Z tails of Ni and Co isotopes.

In first place we find the calibration constants K_1 and K_2 of equation (2.5) and the time offset of equations 2.15. The results are reported in Table 3.4.

Table 3.3: Observed resolution and statistics from the three different ZeroDegree rips for ^{56}Cu . In the first line the resolution is reported in percent, in the second line the respective statistics. These results have been obtained analysing only 50000 events of each acquisition runs.

	rips 8-9	rips 9-11	rips 8-11
res. (%)	0.58	0.28	0.30
stat.	58072	57914	56363

Table 3.4: Calibration constant, values are expressed in a.u.

K_1	K_2	$t_{offset}(57)$	$t_{offset}(911)$
17.5931	-7.1212	302.723	-134.88

To obtain these parameters, it is sufficient to fit the known atomic numbers for some known isotopes with the uncalibrated ones as in the following equation

$$Z = K_1 Z_{uncalib} + K_2. \quad (3.3)$$

The same has been done for the mass-to-charge ratio to obtain the t_{offset} . Calibrated PID spectra are shown in Figure 3.11.

Background in the incoming spectra (Figure 3.11 (a)) is present. This can be explained by the fact that in BigRIPS a much intense particle flux is present and when they pass through the ionization chamber in F7, whose pulse-height signals are slow, this high rate cause a pile-up of the signal, resulting in a higher estimate of the atomic number of the particle [26]. This events can be in part removed requesting correlation between the energy measured in the TEGIC and that measured in the scintillators placed in F3 and F7 but this will cause a loss in statistics. The same arguments hold also in ZeroDegree. The results of these correlations are shown in Figure 3.13, while in Figure 3.12 we show the correlation between TEGIC and plastic detectors.

Inconsistent events can also be effectively removed requesting that PPACs were all fired, in this way we can reduce multi-hit and δ -rays events. PID spectra created with this type of gates are shown in Figure 3.14. With this requirements we obtain a BigRIPS PID with a 11% of statistics on ^{57}Zn respect to the case with no filters. In Figure 3.15 particles per second plot are shown for ^{57}Zn in BigRIPS. In panel (b) a cut on the F3-F5 x-position is applied to reduce contamination in the isotope identification. The flux of ^{57}Zn stays almost constant over the entire experiment, except for few runs

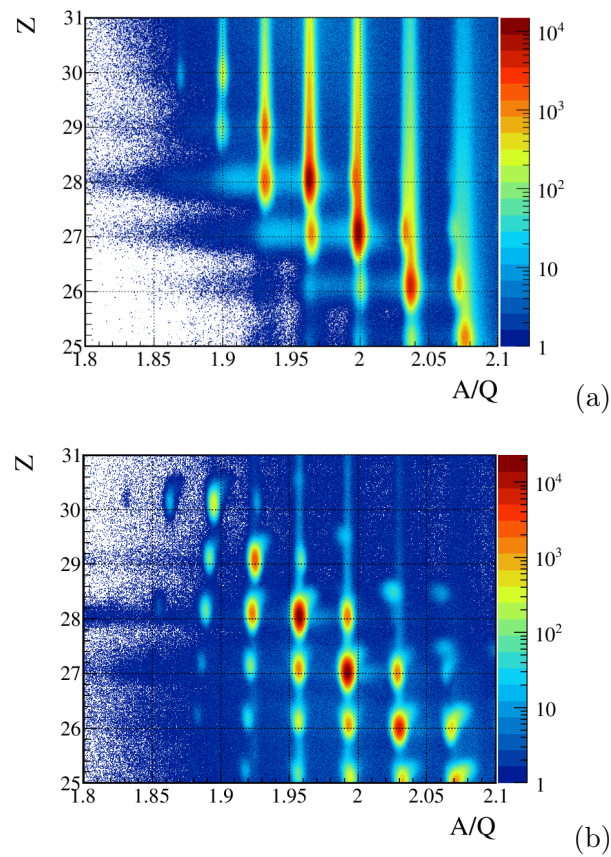


Figure 3.11: Calibrated particle-identification spectra for: (a) incoming particles from the secondary beam and (b) outgoing particles after the interaction with the Beryllium target.

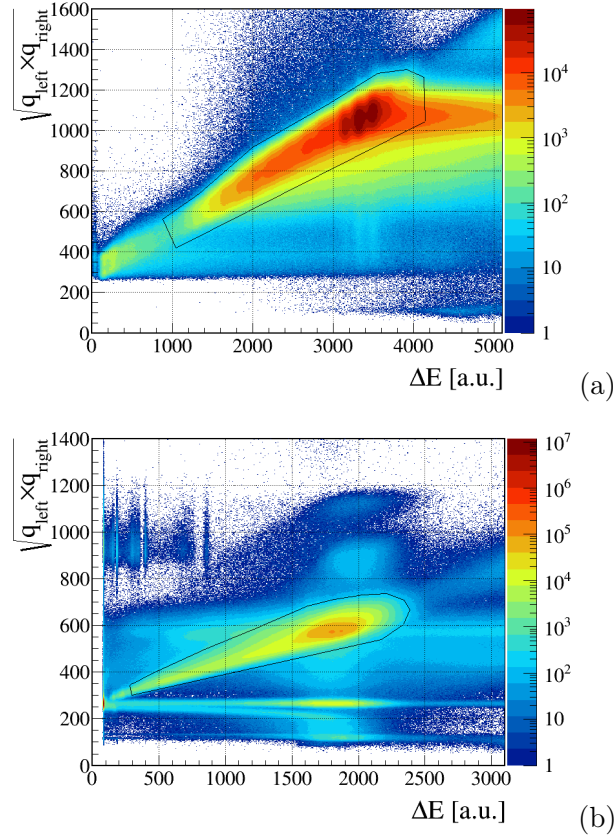


Figure 3.12: Correlation spectra for: (a) F7-TEGIC and F7-plastic and (b) F11-TEGIC and F11-plastic. The lines in black in both panels represent the correlated events. X-axis represents the geometrical average of the ADC signal measured from each anode pairs of each TEGIC, while y-axis is the square root of the product $q_{left} \times q_{right}$ from plastic signals.

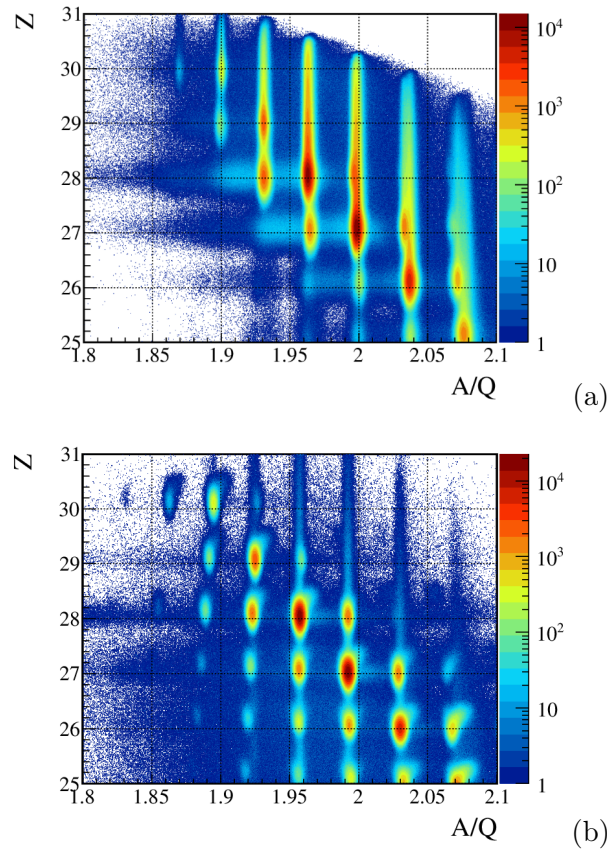


Figure 3.13: PID spectra for (a) BigRIPS with the requirement on correlations between charge-integrated signals in F3 and F7 plastic and energy signals in F7-TEGIC and (b) ZeroDegree assuming correlations between charge-integrated signals in F8 and F11 plastic and energy signals in F11-TEGIC.

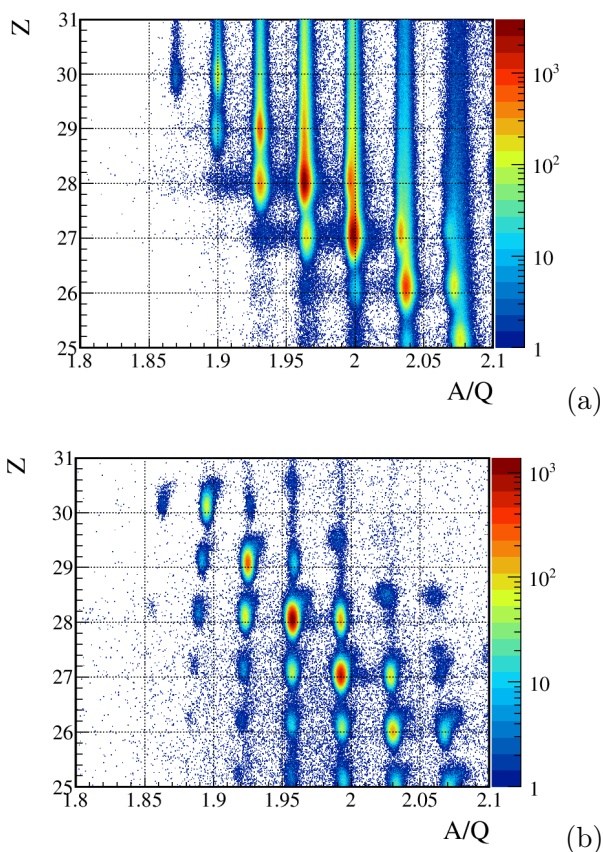


Figure 3.14: PID spectra for (a) BigRIPS with the requirement that all plates in F3 and F7 PPACs were fired and (b) ZeroDegree this time requesting that even all the plates in F9 and F11 were fired.

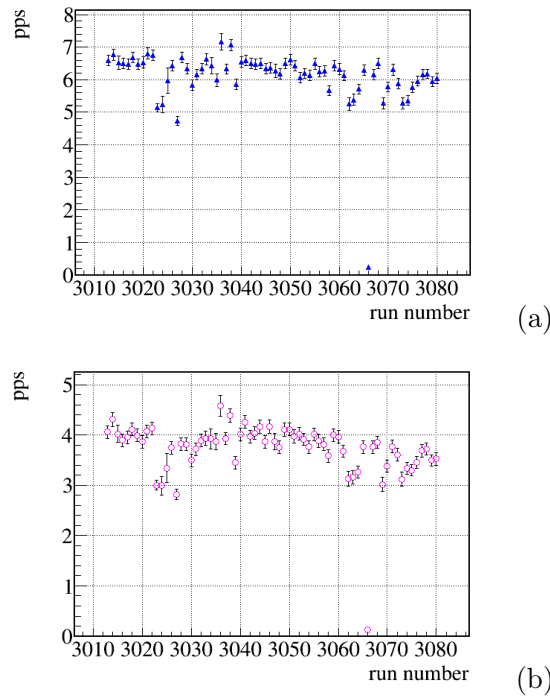


Figure 3.15: Particles per second plots of ^{57}Zn in BigRIPS. In panel (b) a cut on F3-F5 x-position is applied for a cleaner isotope identification, see Section 3.2.3 for details.

which show a decrease in the isotope concentration due to technical issues. We can say thus that about 5 pps of ^{57}Zn were present in the secondary beam.

3.2.1 Charge States

Some of the identified ions are not fully stripped of their electrons. This can happen when ions pass through the detectors on the beamline, in particular traversing the degrader [26]. Ions pick-up one or more electrons, coming out with different Q values. If this happens, it is used to say that the particles have a *charge states*. As a matter of fact, if a particles changes its Q , then also its mass-to-charge ratio changes and consequently the magnetic rigidity, see equation (1.3). These states can be identified more clearly in the ZeroDegree PID, Figures 3.11(b) and 3.13(b), as those blobs with a non-integer value of Z .

In order to remove these events we can simply check the $B\rho$ values. In

Section 3.2 we introduced the concept of "rips", which is briefly the set of reconstructed parameters between two foci. To each rips it is thus assigned the corresponding $B\rho$ value⁴. Plotting the $B\rho$ associated to a certain rips and the $B\rho$ of the next one we can check if the particles changed their states and eventually remove them from the analysis. As an example in Figure 3.16 the case of ^{57}Zn in BigRIPS is reported. In Figure 3.17 the charge states of the outgoing ^{56}Cu in ZeroDegree is shown.

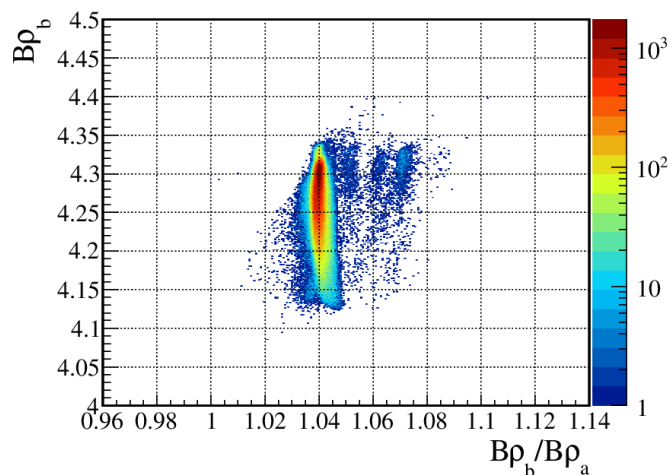


Figure 3.16: Example of charge states in the incoming ^{57}Zn in BigRIPS. The small blobs on the right part of the plot represent these charge states. $B\rho_b$ is the $B\rho$ value reconstructed between F3 and F5 focal planes, $B\rho_a$ is the one reconstructed between F5 and F7. $B\rho$ values are given in Tm .

3.2.2 Reactions

It is now possible to make use of the clean and calibrated PID to estimate which reactions took place at the Beryllium target. This can be obtained by gating the incoming particle identification spectrum on the outgoing isotope of interest. Examples in Figure 3.18 of some of these plots are reported. In Figure 3.18 (b) for what concern the inelastic-elastic channel background is clearly visible. This is due to the inconsistent events acquired by PPACs as mentioned in Section 3.1.2. It also seems that some reactions not physically

⁴For example to the rips 3 to 5 is associated the reconstructed $B\rho$ value between the focal planes F3 and F5, while a different $B\rho$ value correspond to rips 5 to 7, that is the one reconstructed between F5 and F7.

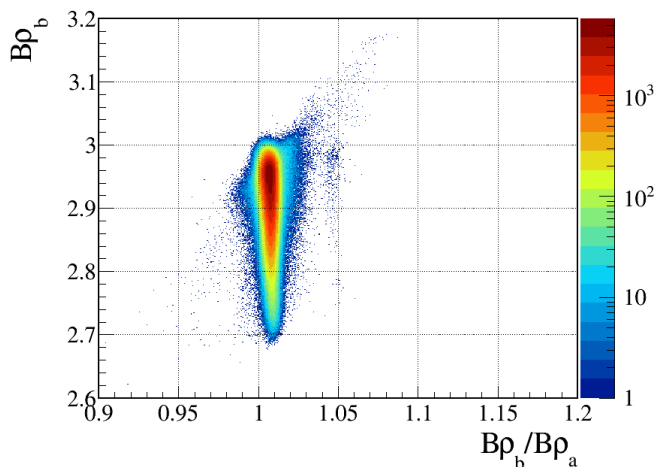


Figure 3.17: Example of charge states in the outgoing ^{56}Cu in ZeroDegree, the small blobs on the right part of the plot represent these charge states. $B\rho_b$ is the $B\rho$ value reconstructed between F8 and F9 focal planes, $B\rho_a$ is the one reconstructed between F10 and F11. $B\rho$ values are given in Tm .

plausible have happened. These are $^{54}\text{Ni} \rightarrow ^{56}\text{Cu}$ and $^{55}\text{Ni} \rightarrow ^{56}\text{Cu}$. The reason is similar to that presented at the beginning of this Section and fundamentally due to the signal pile-up in F11-TEGIC, this is less evident in the ZeroDegree PID but still present. Isotopes like ^{54}Ni due to this pile-up result with an higher Z value and when cuts around ^{56}Cu are made on the ZeroDegree particle identification spectrum, also these isotopes are presented. In the next paragraph a method to clean particle identification is presented. The BigRIPS spectrum gated on outgoing ^{56}Cu will also be reported.

3.2.3 F3 vs F5 position distribution

In this Section a method to overcome the issue of pile-up in the F7-TEGIC detector and then better identify isotopes is reported. This will be used also to evaluate inclusive cross-section in the next Chapter.

It has been said that, because of the pile-up in the F7 ionization chamber, when a cut on the incoming isotope of interest is done, see for example Figure 3.19, impurities coming from other particles with similar A/Q but different Z , are present. A way to reduce these contaminations is to use their different A/Q . In other words, even if they shows higher Z values in the BigRIPS PID, it is possible to separate them using their rigidity, that depends only on their mass-to-charge ratio. To do this the F3 or F7 position distribu-

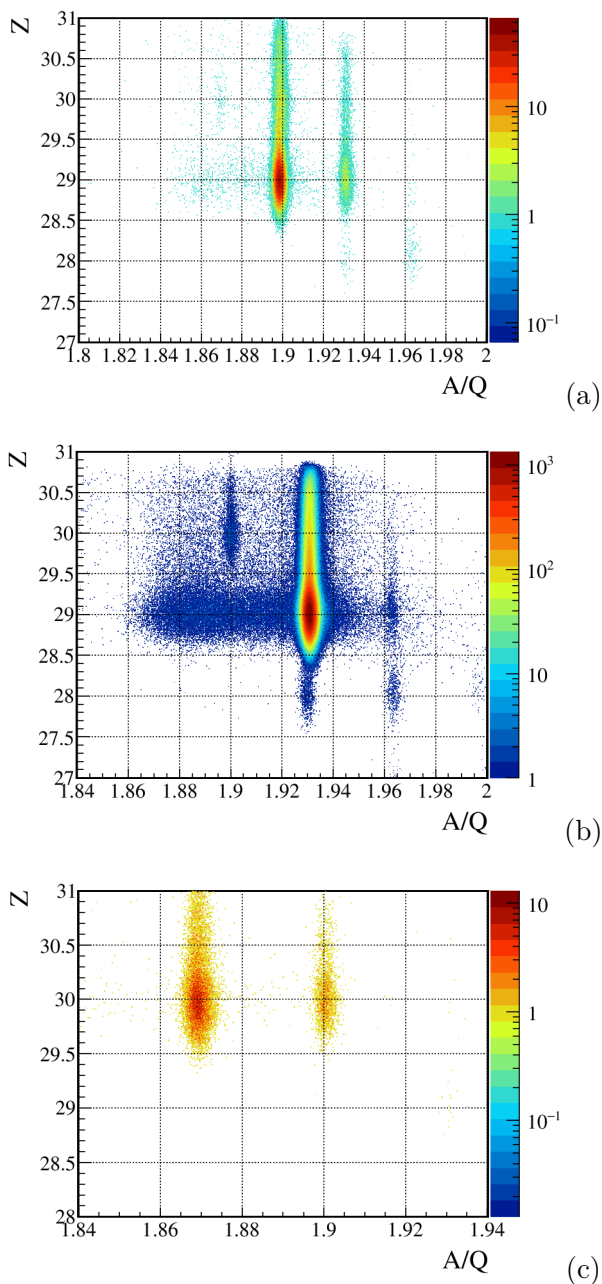
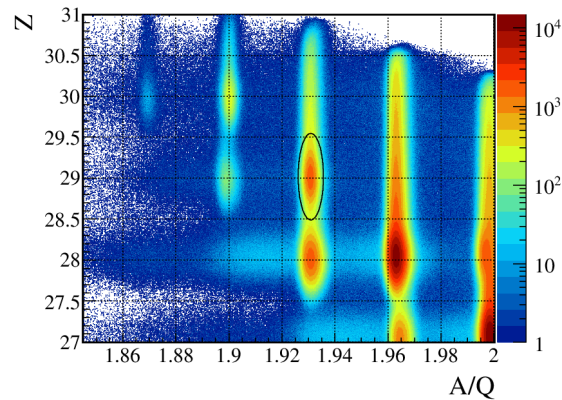


Figure 3.18: (a) Incoming particle identification spectrum gated on outgoing ^{55}Cu : inelastic/elastic channel is clearly visible as also it is the one neutron knockout reaction channel from ^{56}Cu . (b) The same as in (a) but for ^{56}Cu : again inelastic/elastic channel is visible as the one neutron knockout reaction channel from ^{57}Cu and the one proton knockout reaction channel from ^{57}Zn . (c) As in the previous cases incoming PID spectrum this time gated on outgoing ^{56}Zn , it is possible to distinguish the inelastic/elastic channel and the one neutron knockout reaction channel from ^{57}Zn .

Figure 3.19: Example of cut on incoming ^{56}Cu .

tion can be plotted against the F5 position distributions. It is used F3X or F7X because F3 and F7 focal planes are achromatic, while F5 is dispersive, so checking F3X versus F7X will not help to identify contaminations. It has been chosen to use F3X versus F5X simply because for this experiment F3 focal planes shows a more constant efficiency during the runs, see Figure 3.2. In Figure 3.20 these distributions are reported for the isotopes ^{56}Cu , ^{57}Zn and ^{57}Cu .

Referring to this last isotope, ^{57}Cu , without this identification based also on his position distribution, it would not be possible to identify it simply from the particle identification spectrum. In fact, as we can see from Figure 3.11 (a) and Figure 3.13 (a), the contamination is so high and the concentration of the isotope so small, that it is not clearly distinguishable in the incoming channel.

As a proof of the proper isotope identification in the F3-F5 spectrum, we plotted the incoming particle identification spectra with and without these cuts. As an example, Figure 3.21 panel (a) shows part of the BigRIPS PID with the requirement to see only those events with the F3-F5 position distribution that lies inside the cut shown in Figure 3.20 (a). In contrast in panel (b) we demanded to observe only those events with the F3-F5 position distribution that lies outside the cut shown in Figure 3.20 (a). The comparison of the two panels proves the proper isotope identification and also highlights the hypothesis of the high-Z tail contamination.

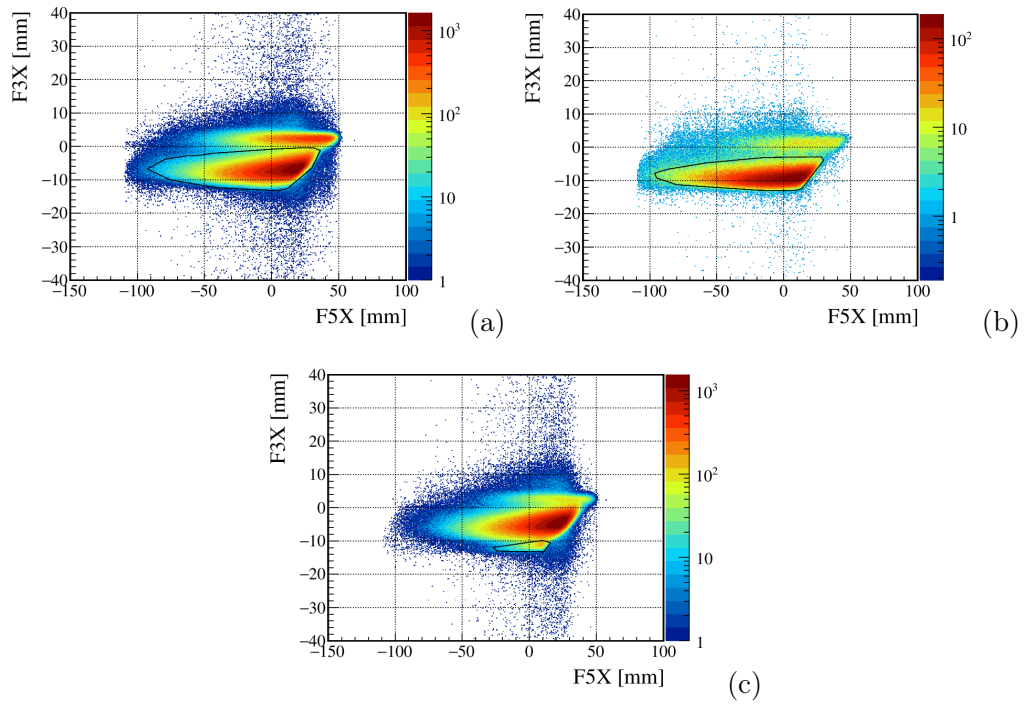


Figure 3.20: (a) F3 position distribution plotted against F5 distribution for the cut reported in Figure 3.19, contaminations respect to pure ^{56}Cu are clearly visible. (b) the same as (a) for the cut on ^{57}Zn . (c) high level of impurities present in the cut on the incoming ^{57}Cu . With black lines in each plot, the cut on the chosen element is shown.

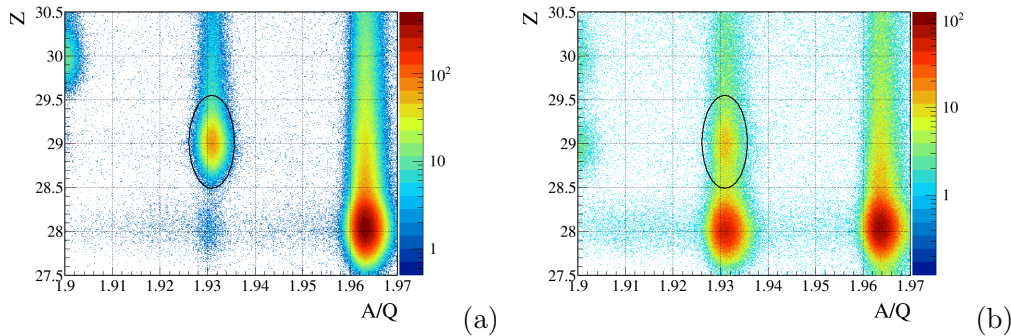


Figure 3.21: Panel (a) reports part of the incoming particle identification spectrum having imposed to see only those events with the F3-F5 position distribution that lies inside the cut shown in Figure 3.20 (a). In panel (b) instead we requested to observe only those events with the F3-F5 position distribution which lies outside the previous cut. In both panels the black line represent the cut on incoming ^{56}Cu . These plots were obtained analyzing only 10^7 events.

3.3 DALI2+ calibration

3.3.1 Energy calibration

This section will be devoted to the description of the calibration of the DALI2+ array, the results of this procedure are also reported. To allow the identification of each DALI2+ detector, an ID running from 1 to 226 has been assigned to each of them and it also depends on the detector position respect to the beamline. In particular the ID increase with the decrease of the detector angle respect to the beamline.

During the experiment, in order to calibrate the array of scintillators detectors, different acquisition runs of ^{137}Cs , ^{60}Co , ^{88}Y and also for the background were performed. In particular each of these spectra have been acquired at the beginning, in the middle and after the end of the physical runs, and we will refer to them as first, second and third set of calibration runs. The sources that have been used are well-known γ -rays emitters: 661.657 keV photons belongs to the ^{137}Cs source, 898.036 and 1836.052 keV photons are emitted from the ^{88}Y and 1173.228 and 1332.492 keV belongs to that ^{60}Co isotope.

Of the 226 detectors, those with the ID 1, 2 and 208 were not operating during the experiment, so automatically they have been excluded from the analysis.

In Figure 3.22 the energy difference between the literature value of the γ -

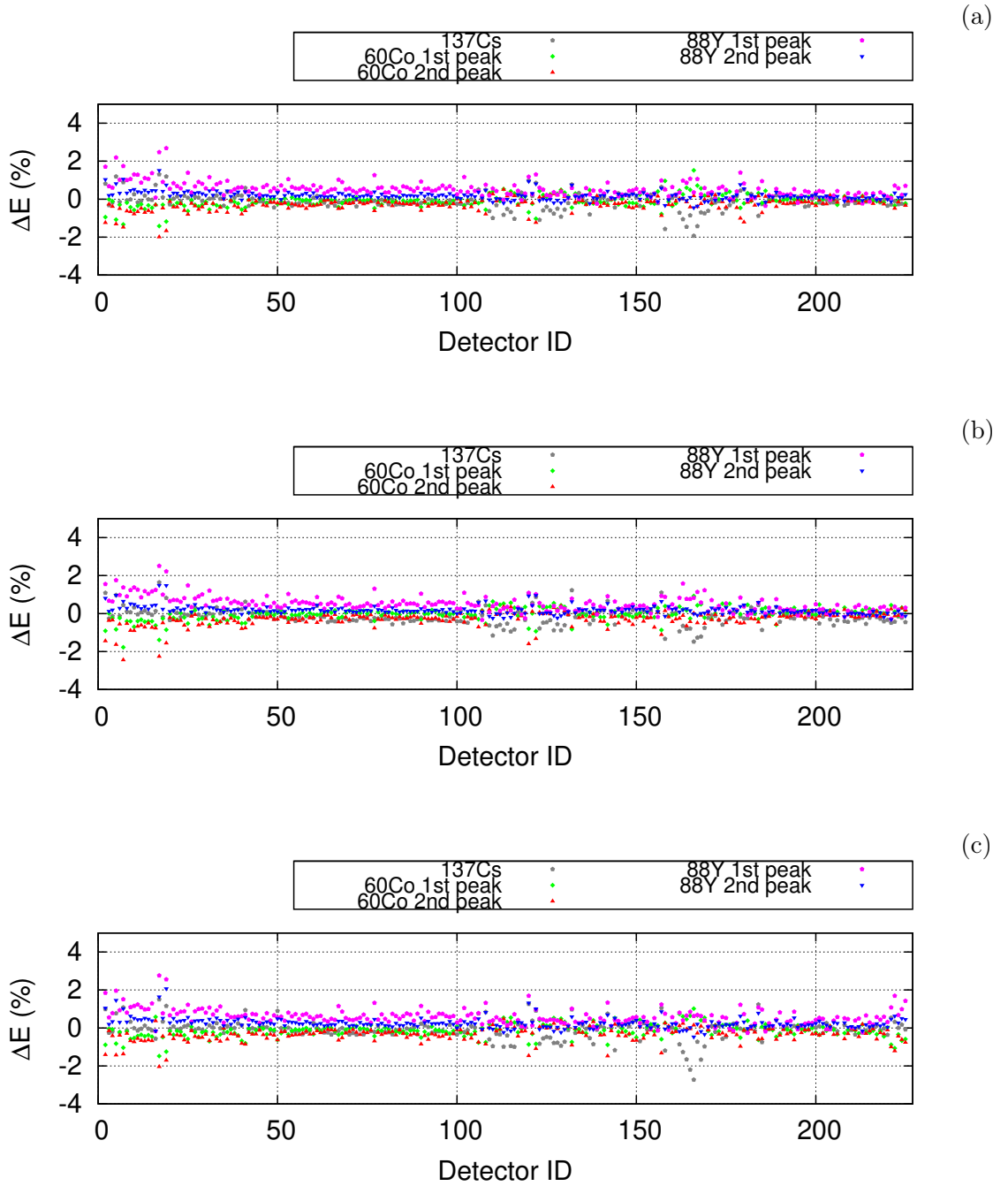


Figure 3.22: Difference between the literature value of the γ -ray emitted from the source and the fitted one after the calibration have been performed for (a) the first set of calibration runs, (b) the second set and (c) the third set after the end of the experiment.

ray emitted from the source and the one fitted after the calibration is reported for the three sets of calibration runs. We find good agreement between the different sets and the energy difference is below the 2% for almost all the detectors except for the ID 8, 18, 166 and 167. The calibration for these last two detectors suffers of the very low statistics acquired from the runs of the Cesium source because of their position in the array respect to the source, while the other two has been removed from the analysis. In Figure 3.23 the detectors resolution obtained for each source and for each calibration set is presented. The first twenty detectors show a lower resolution. This can be explained by the fact that the worst detectors are used in the first layers at backward angles, also detectors with ID from 163 to 170 show an decrease in resolution because the low statistics they have acquired due to the fact that they are shielded by other detectors. Others arguments must be submitted for the ID 113. It exhibits issues to correlate energy and time of some good events. This can be due to some cabling issues, and it results in a cutting of the low energy part of the spectrum as we can see in Figure 3.23 (a), where it is associated with a resolution of 0% for the ^{137}Cs and for the first ^{88}Y peaks because it does not recognize events with energy lower than almost 1 MeV as properly time-correlated.

In order to study the gain drift in DALI2+, the ADC value of the centroid peak for each γ -source was compared between different set of calibration. Then the gain drift is defined as

$$GAIN(\%) = \frac{ADC(peak, set_1) - ADC(peak, set_2)}{ADC(peak, set_1)} \times 100, \quad (3.4)$$

where "peak" refers to one specific emission peak of the source studied and set_1 and set_2 refers to two different and consecutive calibration sets. In Figure 3.24 the results for this drift are reported, in particular in (a) is shown the gain drift for the ^{137}Cs source. In red the drift between the first and the second calibration set is reported, while in green the drift between the second and the third set. In general the gain value is always under the 2% except for some of the first detectors, and for the Cobalt source for the very last ones.

For each detector also the evolution of the Full Width at Half-Maximum (FWHM) with the centroid energy was checked. This relation can be expressed by the formula

$$FWHM = k_1 \times E^{k_2}. \quad (3.5)$$

The obtained values of the fit parameters, k_1 and k_2 , then should be used for the Monte Carlo simulation of the DALI2+ response. In Figure 3.25 the dependence of the resolution on the energy is reported for one of the array

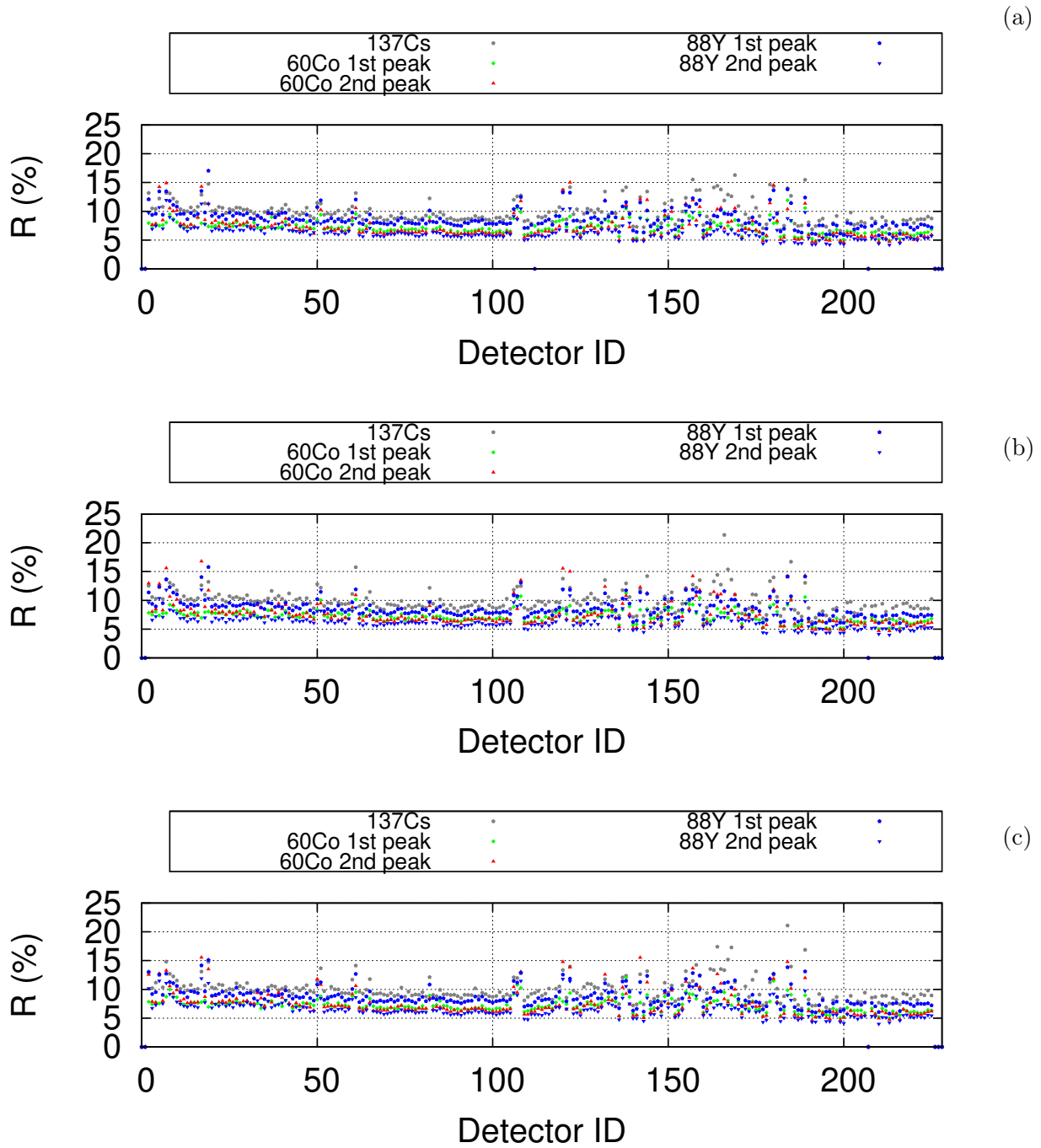


Figure 3.23: Detectors resolution obtained for (a) the first set of calibration runs, (b) the second set and (c) the third set.

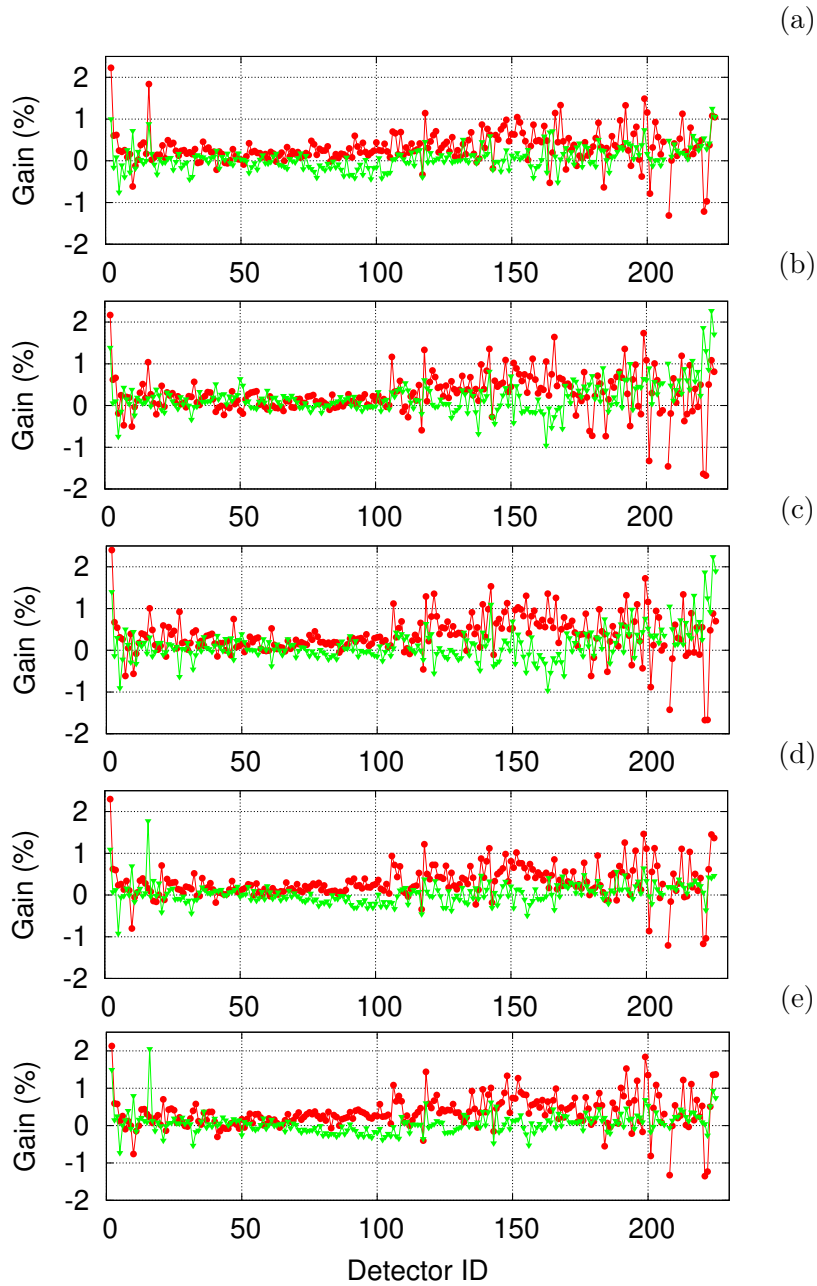


Figure 3.24: Gain drift for (a) ^{137}Cs , (b) ^{60}Co first peak, (c) ^{60}Co second peak, (d) ^{88}Y first peak and (e) ^{88}Y second peak. In red is shown the gain variation from the first to the second set of calibration runs, while in green the drift between the second and the third.

detectors. From the fit, the values of k_1 are in general included between 1 and 6, while k_2 varied between 0 and 1.

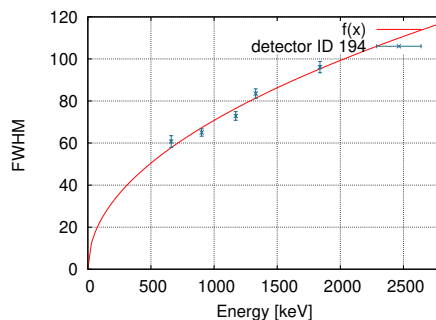


Figure 3.25: Dependence of the FWHM on the energy for one of the DALI2+ detectors.

3.3.2 Time calibration

After having performed the energy calibration, the time signal from each detector needs to be checked. As shown in Figure 3.27 the time signal of each detector after one physical run was fitted with a Landau distribution. The offset parameter obtained then was used to align time signals between

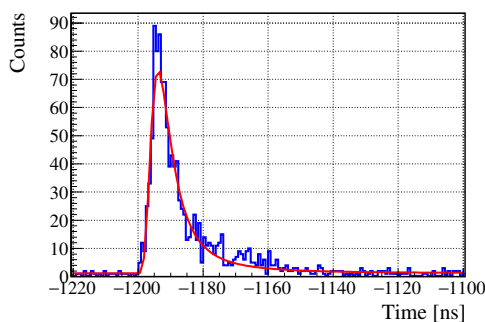


Figure 3.26: Example of time calibration for one of the DALI2+ detectors. In blue is reported the time signal of that detector after one physical run, while in red the fitted function.

each other. In this case, we choose a multiplicity equal to one, that is only the first hit of the multihits TDCs was considered for each detector. The result of the calibration is shown in Figure 3.27 where panel (a) refers to the

time spectrum for each detector before the calibration and here it is clearly visible that the timing signals are not aligned, while panel (b) shows the same spectrum after the calibration. Now the centroids are all shifted to zero, the only exception is for detector ID 208, which shows a broader peak. It was decided to exclude this detector from the analysis.

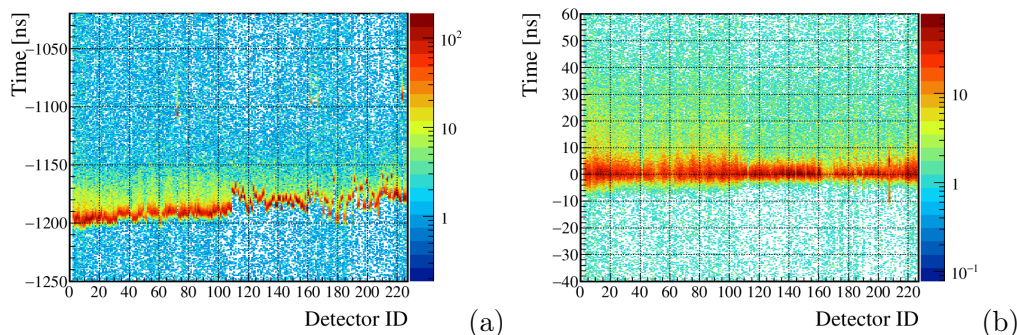


Figure 3.27: Two-dimensional plots of the time signals from each array detector. (a) Time spectrum before the calibration, (b) the same spectrum after having aligned all the crystals to zero.

3.3.3 Background

Background acquisition runs are a very important part of the experiment. Knowing the background sources can help the energy calibration of detectors if for example if we expect a peak from one of the calibration source to fall close in energy to a background peak. If this is the situation, indeed, the source peak will appear broader and the centroid identification biased, resulting in a calibration issue. It is also important to take more than one background acquisition, in order to check if the background composition has changed and as the last step to estimate the background activity. This part is important as well for the detectors efficiency estimation.

During the experiment six background acquisitions were taken. In Figure 3.28 a superposition of the calibration sources energy spectra from one of the calibration sets with that of only background from one of the various acquisition is shown. In this way it is possible to check the validity of the calibration. In panel (a) we can see this superposition for the source spectra obtained from the first set of calibration runs, in panel (b) the same but from the second set and finally, in panel (c) for the third set. For each set the energy calibration is accurate as we can see from the exact superposition of

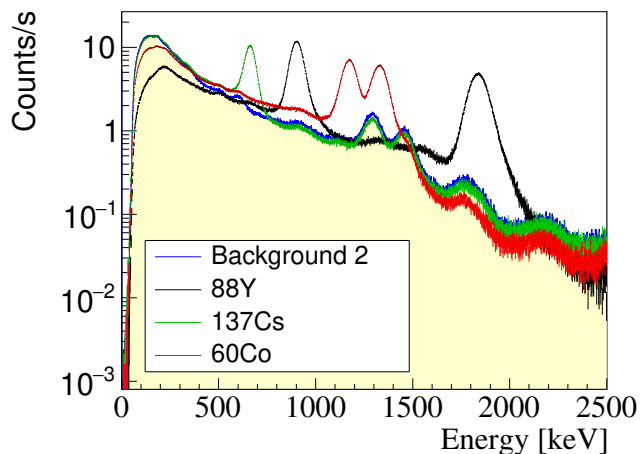


Figure 3.28: Calibrated sources spectra from one of the calibration sets superimposed on the spectrum from one of the background acquisitions. We report in green the ^{137}Cs spectrum, in red the one of the ^{60}Co , in black the acquisition spectrum of ^{88}Y while in blue the background.

the background peaks. It is worth noting that the Cobalt source is affected by the presence of two background peaks around 1290 and 1460 keV. This has sometimes resulted in the broadening of the ^{60}Co peaks, but at the end, it has not affected the resulting calibration significantly.

In Figure 3.29 the spectra from the various background runs are showed all together, in particular panel (b) zooms around the energy region of 1290 keV. This first peak is attributed to the ^{41}Ar activity and it is decaying with time, as expected from that source which has an half-live of 109 minutes. While the second peak around 1460 keV can be attributed to ^{40}K which is a natural background source abundantly present in concrete.

3.4 Doppler-correction

After passing through BigRIPS, the primary beam impinge on the secondary Beryllium target and nuclear reactions take place. If the nuclei emerging from such reactions are produced in excited states, they will emit gamma radiation to de-excite to the ground state. Because the reactions take place while the incident particle is in flight, the γ -rays emitted are Doppler-shifted

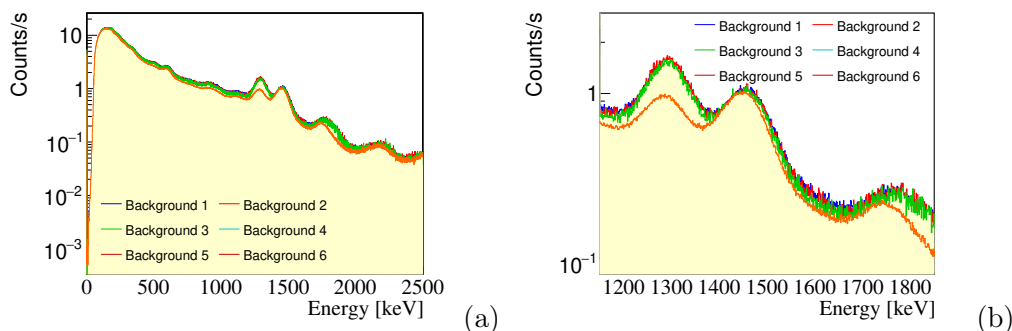


Figure 3.29: Panel (a) shows a superposition of the background spectrum from the six different acquisition runs, while in panel (b) the same plot is zoomed, to make more visible how the count rate of the first peak around 1293 keV belonging to the ^{41}Ar .

according to

$$E_0 = E_\gamma \frac{1 - \beta \cos \theta}{\sqrt{1 - \beta^2}}, \quad (3.6)$$

where E_0 is the real γ -ray energy while E_γ the measured one, βc is the velocity of the incident particle and θ the angle between the direction of the incident particle and the emitted γ radiation.

In order to correct the measured energies, we must know the correct value of the velocity when the reaction has taken place. In principle we can approximate βc with the velocity of the incident particle at half the length of the target. This implicitly requires also the exact determination of the length of the secondary target. After having determined these parameters, a Monte Carlo simulation has to be done in order to reproduce the response of the DALI2+ detectors and the lineshapes associated to the various reaction channels. This goes beyond the scope of this work. For the studied reactions, we have done a preliminary Doppler-correction making the approximations of a 6 mm target length and we recreate Doppler-corrected spectra varying β and taking as the good one, that with the peaks with smallest resolution. These results will be presented at the end of Chapter 4.

3.4.1 Add-back procedure

The add-back procedure is used in the analysis to recover the full energy peak for events in which the γ has deposited its energy in more than one detectors. There are different parameters that have to be chose before doing

this reconstruction and these are the *add-back radius* that is the maximum distance between two different crystals to use both for the reconstruction and the maximum number of crystal that we can use for one reconstruction. For this analysis we choose 15 cm for the radius and 30 as the maximum number of DALI2+ crystal to sum. The results with and without this procedure will be presented and discussed in Chapter 4.

Chapter 4

Experimental results and discussion

This chapter will be devoted to the presentation and discussion of the experimental results obtained applying the data analysis procedure described in Chapter 3. In Section 4.1 *inclusive* cross sections for several reactions are presented. This is the first result here presented, preliminary to the study of the gamma spectroscopy of the populated nuclei.

Once, for a specific reaction the intensity of the gamma transitions are measured, it will be possible to obtain the cross section to a particular excited state. Such cross sections are called “exclusive” cross sections. Experimental values of the inclusive cross section can provide useful insight into the nuclear structure, to be compared with theoretical calculations [34]. Comparison of theory and experiment is possible, provided that some correction are applied. For example it has been suggested that theoretical and experimental cross sections ratio, $R_s = \sigma_{exp}/\sigma_{th}$ depends linearly on the difference of the neutron and proton separation energies, defined as $\Delta S = S_n - S_p$ or as $\Delta S = S_p - S_n$ for neutron and proton removal respectively [35, 36].

4.1 Inclusive cross sections

Inclusive cross sections can be defined as

$$\sigma = \frac{N_{out}}{nN_{in}}, \quad (4.1)$$

where N_{out} represent the number of outgoing particles of that particular reaction channel, N_{in} the total number of incoming particles and n the number of scattering centers, that is $n = \rho_t d_t N_A / m_t$ with ρ_t , m_t and d_t respectively

the density, molar mass and length of the target and N_A is the Avogadro constant.

Starting from equation (4.1), we have to modify it to take into account particles propagation through the beamline. Not all the incoming particles of a particular isotope will reach the secondary target, or if they will reach it, they can not arrive to the end of the ZeroDegree spectrometer and they will be lost. We can define a *transmission coefficient* that gives us an estimate of the particle loss during the propagation [37], [38], [39]. It is defined as

$$T = \epsilon_{line}\epsilon_{target}\epsilon_{zd}, \quad (4.2)$$

where

- ϵ_{line} represents the losses due to the scattering of incoming particle through the beamline in BigRIPS and it is also related to the detectors efficiencies. It can be estimated acquiring runs without the target as $\epsilon_{line} = N'_{out}/N'_{in}$, where N'_{out} and N'_{in} are the outgoing and incoming particles detected in BigRIPS and ZeroDegree. This efficiency should be independent on the reaction channel considered [39].
- ϵ_{target} represent the loss due to the scattering in the target. Its value can not be obtained alone, but the product $\epsilon_{line} \times \epsilon_{target}$ can be estimate from runs with the target included.
- ϵ_{zd} represent the loss due to the ZeroDegree acceptance and it is defined as

$$\epsilon_{zd} = \frac{N'_{out}}{N'_{in} a_{scale}}, \quad (4.3)$$

where a_{scale} is the scaling factor between the F5-position distributions of the incoming and outgoing nuclei.

Equation (4.2) now becomes

$$\sigma = \frac{N'_{out}}{nN'_{in}T}. \quad (4.4)$$

where $N_{out} = N'_{out}/T$.

In our case the product $\epsilon_{line} \times \epsilon_{target}$ was obtained from the F5 x-position distribution. In Figure 4.1 these distributions are shown for different nuclei. As an example in Figure 4.1(a) the case of ^{56}Cu is presented. In blue it is shown the F5 distribution for ^{56}Cu selected in BigRIPS while in red the same distribution is shown but for the unreacted ^{56}Cu selected in ZeroDegree. The bottom part of Figure 4.1(a) represents the ratio between these two

Table 4.1: Product of $\epsilon_{line} \times \epsilon_{target}$ for different isotopes.

<i>Nucleus</i>	$\epsilon_{line} \times \epsilon_{target}$
^{55}Cu	0.776(6)
^{56}Cu	0.707(1)
^{56}Zn	0.699(14)

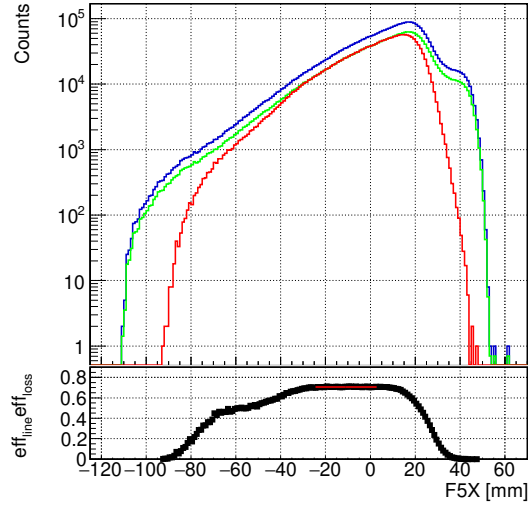
distributions. We define the $\epsilon_{line} \times \epsilon_{target}$ as the value of the constant part of this ratio because this part is independent on the ZeroDegree acceptance, indeed in this region $\epsilon_{zd} = 1$. Finally in the upper part of Figure 4.1(a), in green is shown the F5 distribution for ^{56}Cu selected in BigRIPS scaled by the obtained value of the product of efficiencies.

In the same way it is possible to obtain the ZeroDegree acceptance for the different reactions. In Figure 4.2 F5 x-position distributions are reported for the one-neutron knockout reactions: (a) $^{56}\text{Cu} \rightarrow ^{55}\text{Cu}$ and (b) $^{54}\text{Co} \rightarrow ^{53}\text{Co}$. In the upper part of the plots, in blue it is shown the F5 distribution of the incoming nucleus selected in BigRIPS, in red the one of the outgoing reaction product selected in ZeroDegree, and in green again the incoming nucleus distribution scaled by the factor a_{scale} . This coefficient is obtained fitting with a constant the ratio of the red and blue distributions, as shown in the bottom part of the plots. This a_{scale} is then used in equations (4.3) in order to find ϵ_{zd} .

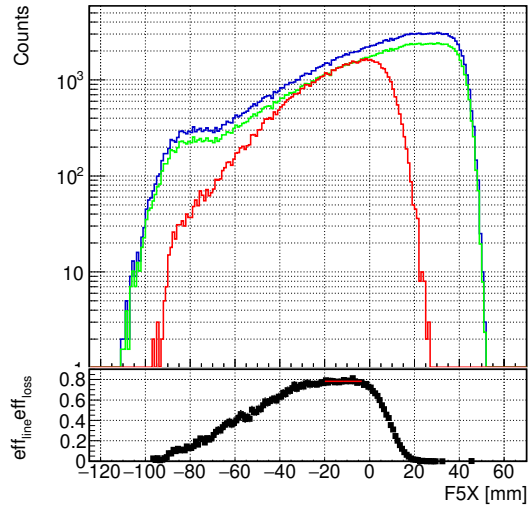
In calculating these efficiencies, events with the fbit trigger equal to 6¹ have been excluded because they do not contain the fbit=1 (the F7-down scaled), as, instead, the others triggers do. So it is inconsistent to make a comparison between events only seen in BigRIPS, which have fbit=1, and events with fbit=6. We used the condition that fbit has to be equal to 1 or 3 or 7.

In Table 4.2 the values of the ZeroDegree efficiencies are reported together with the transmission coefficient T and of the inclusive cross section for all the one-neutron knockout reactions that were measured.

¹In Chapter 3 we have introduced the concept of physical triggers provided by the coincidence module. In particular an fbit value equal to 6 can be obtained only by the combination shown in Table 3.1 which does not contain the F7(DS). Instead fbit values equal to 1, 3 and 7 are conditioned by a F7(DS) event.

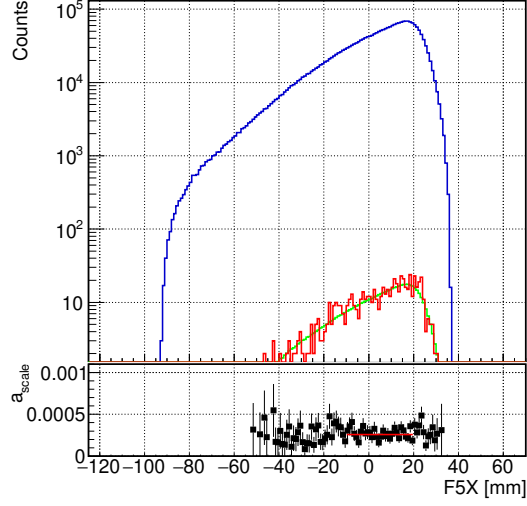


(a)

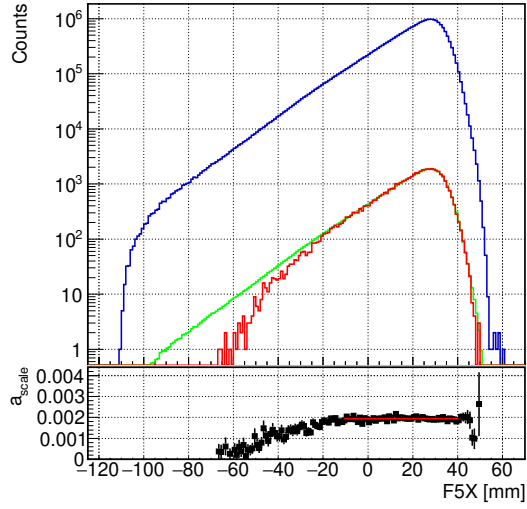


(b)

Figure 4.1: F5 x-position distribution for different nuclei: (a) F5X for ^{56}Cu and (b) F5X for ^{55}Cu . In blue it is shown the F5 distribution for the incoming isotopes selected in BigRIPS while in red the same distribution is shown for the outgoing nucleus selected in ZeroDegree. In green the incoming (blue) distribution scaled to the outgoing (red) one is reported.



(a)



(b)

Figure 4.2: F5 x-position distribution for different reactions: (a) F5X for $^{56}\text{Cu} \rightarrow ^{55}\text{Cu}$ and (b) F5X for $^{54}\text{Co} \rightarrow ^{53}\text{Co}$. In blue it is shown the F5 distribution for the incoming nucleus selected in BigRIPS, in red the distribution for the outgoing nucleus selected in ZeroDegree, while in green the is reported the distribution for the incoming nucleus scaled by the scaling factor a_{scale} .

Table 4.2: Transmission coefficient and ZeroDegree efficiencies for some of the one neutron knock-out reactions.

<i>Reaction</i>	ϵ_{ZD}	<i>Transmission</i>
$^{56}\text{Cu} \rightarrow ^{55}\text{Cu}$	0.99(8)	0.793(2)
$^{55}\text{Ni} \rightarrow ^{54}\text{Ni}$	0.981(7)	0.76776(4)
$^{54}\text{Co} \rightarrow ^{53}\text{Co}$	0.988(6)	0.73926(3)
$^{57}\text{Zn} \rightarrow ^{56}\text{Zn}$	0.96(23)	0.829(8)

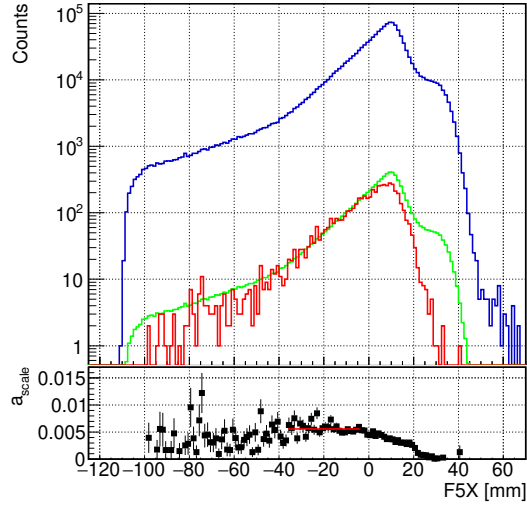
Using the procedure described above, we have calculated the cross sections also for all the other reaction channels. Some of the calculations are much more affected by uncertainty, mostly because the statistics of those processes is scarce and because of the difficulty in isolating a particular isotope when increasing the A/Q ratio for a fixed Z value.

In Figure 4.3 examples of contaminated cross section is shown, while in Figure 4.4 the same distributions are reported, this time having gated in the F3-F5 position distributions in order to clean them as explained at the end of Section 3.2 in Chapter 3. In Figure 4.3 (a) F5 x-position distribution for the one proton knock-out reaction $^{55}\text{Co} \rightarrow ^{54}\text{Fe}$ is presented, while in Figure 4.4 (a) we can see the same reaction after a gate on F3-F5 distributions. In this case, the change in the inclusive cross-section value before and after the gate is considered during the estimate of the systematic error.

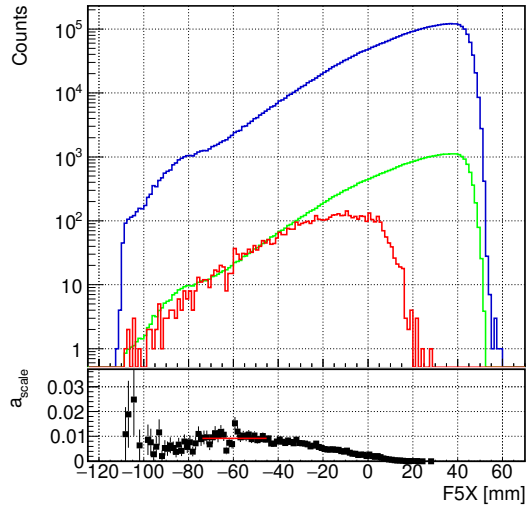
In Figure 4.3 and Figure 4.4 panel (c) the proton knock-out from ^{54}Ni to ^{53}Co is shown without and with the gate on F3-F5 distribution respectively.

In Table 4.3 the calculated cross-sections estimates for various reaction channels are reported. The systematic error was evaluated from one of the reaction with the biggest statistics, in this case the one-neutron knock-out from ^{54}Co . It was calculated repeating the procedure described above for achieving the inclusive cross-sections, although not on the entire set of data but on groups of two runs. From the values obtained the standard deviation was extracted and it was taken as an estimate of the systematic error. To this estimation we added a 2% of uncertainty coming from the target thickness². For the estimation of the cross-sections more affected by the contamination

²It is worth stressing that further error for the one-neutron knockout cross-sections can also arise when those type of reactions take place before the target, in any beamline detector placed after the first double PPAC in F7. This arise from the fact that after the reaction the changes in β and in the $B\rho$ are not sufficient to identify the reaction product with its proper A/Q and Z in BigRIPS.

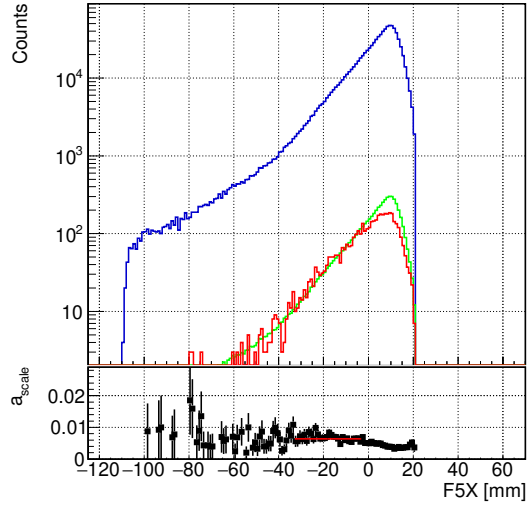


(a)

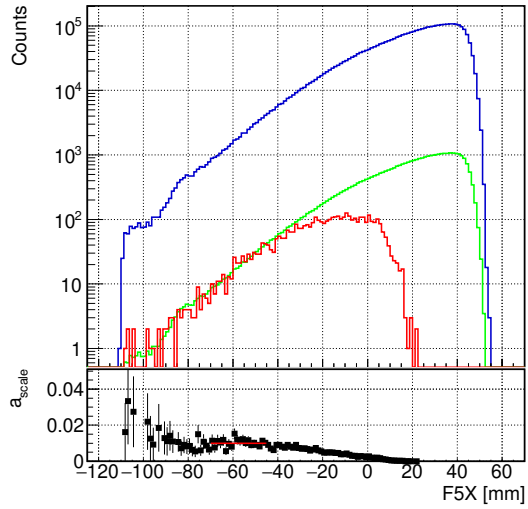


(b)

Figure 4.3: F5 x-position distribution for different reactions: (a) F5X for $^{55}\text{Co} \rightarrow ^{54}\text{Fe}$ and (b) F5X for $^{54}\text{Ni} \rightarrow ^{53}\text{Co}$. In blue it is shown the F5 distribution for the incoming nucleus selected in BigRIPS, in red the distribution for the outgoing nucleus selected in ZeroDegree, while in green it is reported the distribution for the incoming isotope scaled by the factor a_{scale} .



(a)



(b)

Figure 4.4: F5 x-position spectra for the same reactions as in Figure 4.3 after having gated on F3-F5 momentum distributions. In blue it is shown the F5 distribution for the incoming nucleus selected in BigRIPS, in red the distribution for the outgoing nucleus selected in ZeroDegree, while in green it is reported the distribution for the incoming isotope scaled by the factor a_{scale} .

4.1. INCLUSIVE CROSS SECTIONS

Table 4.3: Inclusive cross section values for different reactions. *The first error in parenthesis is statistical, second is systematic. In the third column experimental cross section values from other publications are reported.

Reactions	σ_{exp} [mbarn]	$\sigma_{literature}$ [mbarn]
$^{57}\text{Zn}(-n)^{56}\text{Zn}$	9.3(7)(8)*	
$^{56}\text{Cu}(-n)^{55}\text{Cu}$	4.5(2)(4)	
$^{56}\text{Ni}(-n)^{55}\text{Ni}$	47.0(9)(41)	38.0(2)(30) [40]
$^{55}\text{Ni}(-n)^{54}\text{Ni}$	28.9(1)(21)	
$^{55}\text{Co}(-n)^{54}\text{Co}$	44.2(9)(39)	39.0(4)(28) [41]
$^{54}\text{Co}(-n)^{53}\text{Co}$	35.0(2)(30)	
$^{54}\text{Fe}(-n)^{53}\text{Fe}$	64.6(19)(57)	
$^{53}\text{Fe}(-n)^{52}\text{Fe}$	66.5(4)(58)	
$^{56}\text{Cu}(-p)^{55}\text{Ni}$	229(3)(20)	
$^{56}\text{Ni}(-p)^{55}\text{Co}$	98(2)(9)	126(2)(17) [40]
$^{54}\text{Ni}(-p)^{53}\text{Co}$	166(2)(15)	
$^{55}\text{Co}(-p)^{54}\text{Fe}$	114(2)(15)	141(3)(16) [41]
$^{54}\text{Co}(-p)^{53}\text{Fe}$	106(1)(15)	
$^{55}\text{Ni}(-pn)^{53}\text{Co}$	72.0(3)(62)	
$^{54}\text{Co}(-pn)^{52}\text{Fe}$	134(1)(32)	
$^{55}\text{Ni}(-pn)^{53}\text{Fe}$	56(1)(9)	
$^{56}\text{Cu}(-2pn)^{53}\text{Co}$	45(1)(4)	
$^{55}\text{Ni}(-2pn)^{52}\text{Fe}$	73(1)(6)	
$^{55}\text{Co}(-p2n)^{52}\text{Fe}$	18.8(24)(11)	

on the identification of the nucleus, the difference³ in the cross-section value obtained with and without gating on F3-F5 distributions is included in the estimate of the systematic error [40].

The values obtained are compared with literature cross sections estimates whenever it is possible. In those cases reported, the obtained values are favourably comparable with the previous publications.

In Figure 4.5 panel (a) we report the calculated one-neutron knockout cross-sections as a function of the proton separation energy S_p of the reaction products. An overall increase in the cross-section values is clearly visible. The closer S_p is to zero, the larger is the probability of that nucleus to decay

³ This has been done only in the cases in which this difference was bigger the systematic error.

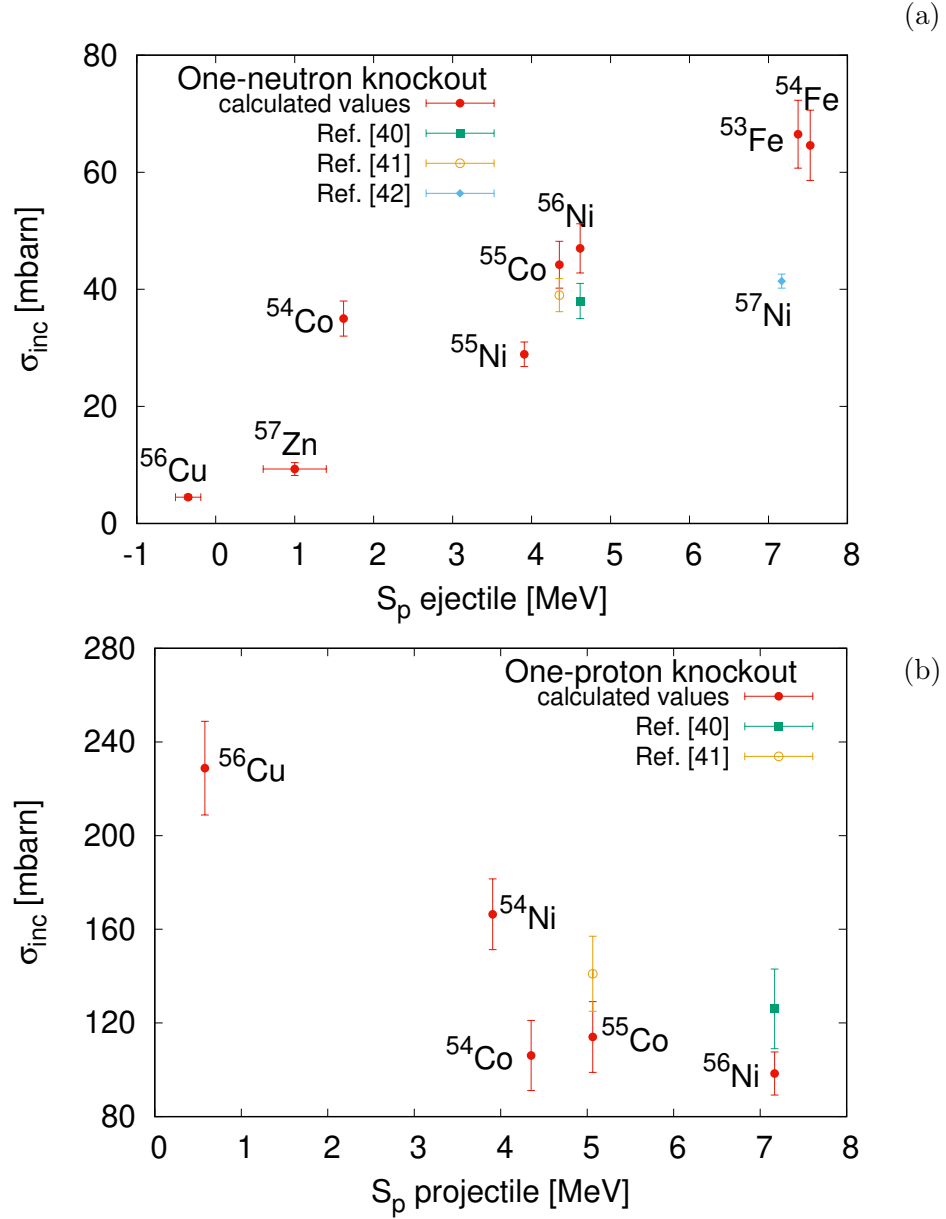


Figure 4.5: Panel (a) reports the measured one-neutron knockout cross-section values (red filled circle) listed in Table 4.3 as a function of proton separation energy of the ejectile. Literature values are taken from Ref. [41] for ^{55}Co (orange open circle), Ref. [40] for ^{56}Ni neutron knockout (green filled square) and Ref. [42] for ^{57}Ni (light blue filled diamond). In panel (b) the calculated one-proton knockout cross-sections are shown as a function of the projectile proton separation energy. Literature values are taken from Ref. [41] for ^{55}Co (orange open circle), Ref. [40] for ^{56}Ni proton knockout (green filled square). In both panels the projectile is also indicated. The S_p values are taken from Ref. [43] for ^{56}Cu while from Ref. [44] for the other nuclei.

emitting a proton. This implies that the probability to populate a resonance that lie above the proton separation energy will increase. This directly translates in a reduction of the cross-section. It is worth stressing that even if the ^{55}Cu is unstable to proton emission ($S_p < 0$), its proton separation energy value is sufficiently close to zero that the Coulomb barrier for the proton prevents the proton decay of the ground state.

The observed cross-sections dependency on the S_p is in agreement with the result obtained by Paul, Obertelli and others in Ref. [45]. They studied neutron-rich nuclei, in particular the effects of pairing correlations in inclusive one-proton and one-neutron cross-sections. As shown in Figure 3 panel (a) of that work, they observed an overall increase of the inclusive one-proton knockout cross-sections as a function of the ejectiles neutron separation energy. In particular they observed that the inclusive one-proton knockout cross-sections for even- Z projectiles show a systematic enhancement relative to odd- Z projectiles for the same S_n of the ejectiles.

In panel (b) measured one-proton knockout cross-sections are shown as a function of the proton separation energy of the projectiles. We used the S_p of the reacting nuclei because it is an estimation of how much these nuclei are stable against proton emission. We thus can expect an overall decrease of the cross-sections with the increase of S_p . This arises from the fact that we are going from exotic proton-rich nuclei near the proton drip line toward nuclei close to $N=Z$.

Comparing the magnitude of the inclusive one-neutron and one-proton knockout cross-sections, we observe that the second has systematically higher estimates for the same projectiles as an indication that nuclei tend to move towards a more stable configuration reducing the neutron-proton asymmetry.

At the beginning of this Chapter we introduced the experimental observation of the existence of a *reduction factor* between theoretical and experimental values of cross-sections. From the Figure 1 of the work of Tostevin and Gade [36] a R_s of 0.4 can be extracted [46] for the one-neutron knockout inclusive cross-section from ^{57}Zn . This value of the reduction factor and our cross-section estimate of 9.3(7)(13) mbarn are in agreement with the preliminary theoretical calculations performed for this experiment using the ANTOINE code [47] and the KB3G [48] effective interaction [46].

4.2 Doppler-correction of γ -transitions

In this Section the last step of the analysis is presented, the study of the γ radiation emitted by the nuclei that have reacted with the secondary target. In this Section only preliminary results are presented.

The Doppler-corrected energy of the gammas emitted by a particular nucleus enable the study of the excited levels that were populated and their cross-section. This is particular important for nuclei with a level scheme still unknown. The isotopes ^{55}Cu and ^{56}Cu were analyzed. They are the most exotic proton-rich nuclei populated with sufficient statistics during the experiment and their level scheme is still unknown. The first, ^{55}Cu , is a $T_z=-3/2$ nucleus and together with ^{55}Fe it forms a mirror pair. The other isotope of Copper, ^{56}Cu , has $T_z=-1$ and its mirror nucleus is ^{56}Co . The level schemes of ^{55}Fe and ^{56}Co are known from experiments.

Before checking the γ spectra of the more exotic proton-rich nuclei belonging to these three mirror pairs, we studied the gamma radiation emitted by nuclei with a known level scheme which were populated during the experiment. We analysed the spectra of ^{54}Fe , populated by one-proton knockout from ^{55}Co and that of ^{52}Fe , populated by one-neutron knockout from ^{53}Fe . In Figure 4.6, 4.7 and 4.8 spectra of gamma radiation emitted from these nuclei is reported. The spectra were obtained following the procedure presented in Chapter 3 and already include the add-back procedure except for that of Figure 4.6 panel (b). Figure 4.6 panel (a) represents a two-dimensional plot of the Doppler-corrected γ energy spectrum for the ^{52}Fe isotope as a function of detector ID. In panel (b) the same spectrum is shown in the laboratory system. The drift of the peaks is clearly visible. In the laboratory system the detectors cover a large range of angles⁴ and those positioned at backwards angles measure an E_γ that is higher in value respect to the true value, see equation (3.6). Increasing the detector ID and thus decreasing its angle respect to the beamline, we instead obtain γ energies that will be lower in value respect to the true energy. In this panel a peak at 511 keV is visible. The constancy of its measured energy among all the detectors belongs to the fact that this is emitted at rest. This peak is typical for proton-rich radioactive beams which, after scattering and positron decay in and near the target chamber, give rise to a high background from 511 keV photons [49]. When we perform a doppler-correction, this peak will be shifted to an energy value that depends on the detector position. In panel (a) the 511 keV peak is recognizable as that peak which energy goes from 720 keV for the first detectors to almost 308 keV for those with the highest ID.

In Figure 4.7 the case of ^{54}Fe is shown. The energy of the peaks reflect the transitions from $J=4^+$ to $J=2^+$ for the first peak and from $J=2^+$ to $J=0^+$ for the second peak [50, 51]. In Figure 4.8 the case of ^{52}Fe is reported. The first peak at 849 keV belongs to a $J=2^+$ to $J=0^+$ transition, while the second peak at 1535 keV can be attributed to a $J=4^+$ to $J=2^+$ decay [51, 52, 53].

⁴See Section 2.4 of Chapter 2 for details.

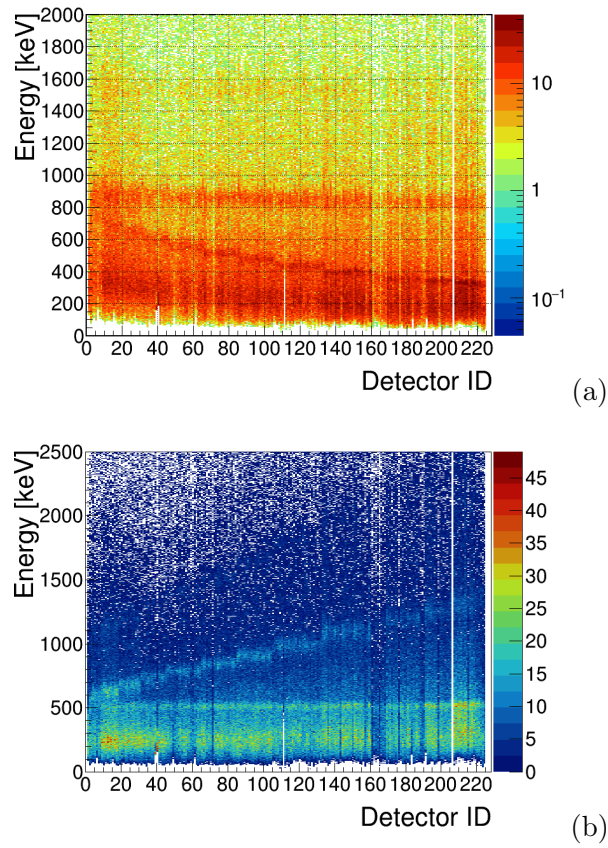


Figure 4.6: In panel (a) the two-dimensional plot of the preliminary Doppler-corrected γ energy spectrum for the ^{52}Fe isotope as a function of detector ID is shown. In panel (b) the same spectrum is shown in the laboratory system. Each bin on the y-axis represents 5 keV.

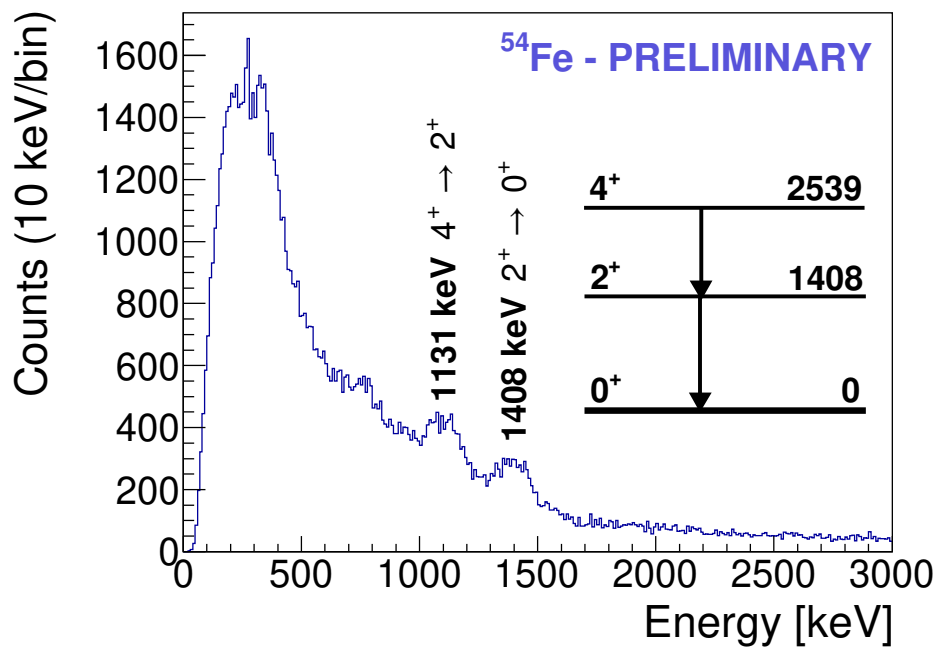


Figure 4.7: The preliminary spectrum obtained from the gamma radiation emitted from ^{54}Fe populated by the one-proton knockout from ^{55}Co is shown. Each bin represents 10 keV.

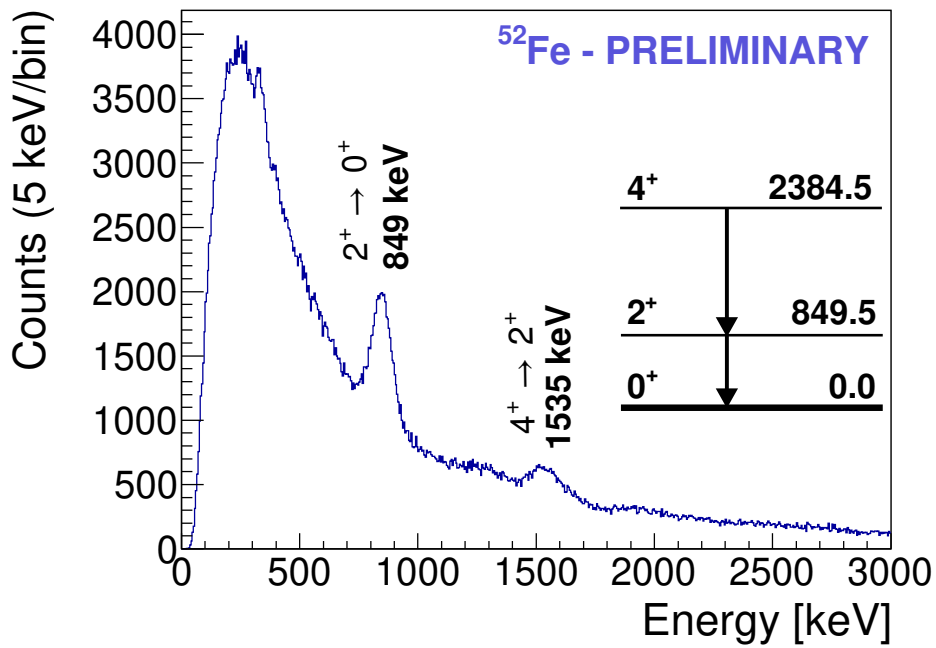
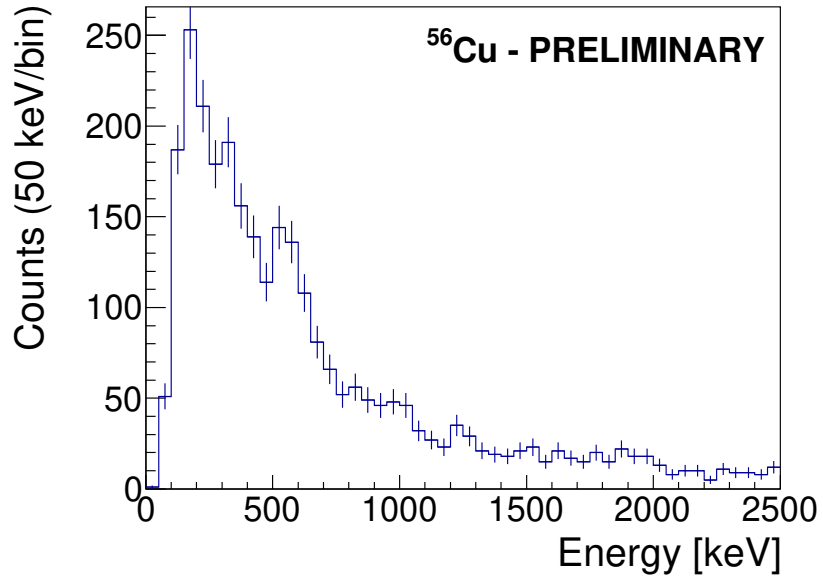
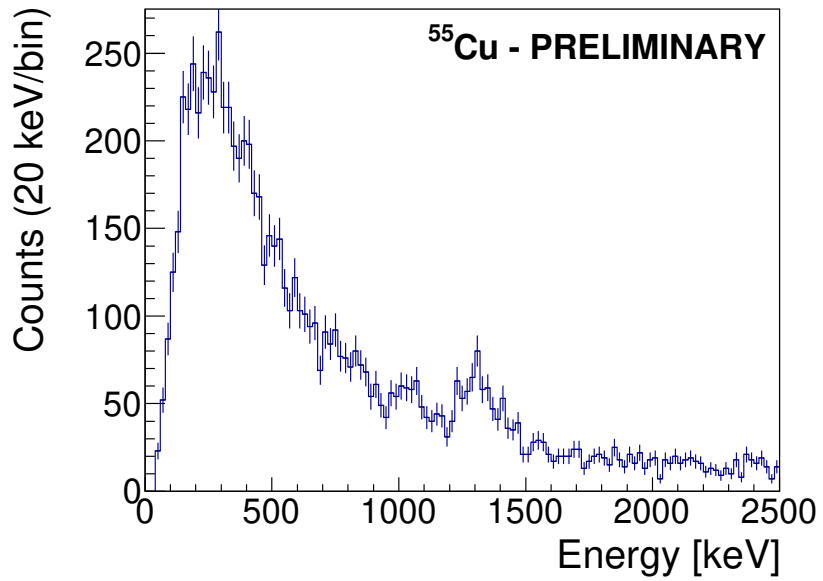


Figure 4.8: The preliminary spectrum obtained from the gamma radiation emitted from ^{52}Fe following the one-neutron knockout from ^{53}Fe . Each bin represents 5 keV.



(a)



(b)

Figure 4.9: Spectra of gamma radiation emitted by: panel (a) ^{56}Cu and panel (b) ^{55}Cu . The binning is 50 keV/bin and 20 keV/bin respectively.

4.2. DOPPLER-CORRECTION OF γ -TRANSITIONS

In Figure 4.9 panel (a) we report γ spectra obtained from ^{56}Cu populated from ^{57}Zn one-proton knockout, here a peak at about 570 keV is visible. In panel (b) γ spectra from ^{55}Cu populated from ^{56}Cu one-neutron knockout, is shown. A peak around 1330 keV can be identified.

Chapter 5

Conclusions

This last Chapter will be devoted to briefly summarise the procedure and the results obtained during the analysis.

The aim of the experiment analyzed is to study exotic proton-rich nuclei as ^{56}Zn and ^{55}Cu . Nowadays there are no experimental results regarding excited states for these nuclei, except for the ones we presented in this work. These nuclei are of particular importance to improve our understanding on the isospin symmetry. They are far apart from $N=Z$ nuclei, member of isospin multiplets with $T=2$ and $T=3/2$, respectively, and this makes them the ideal candidates for these kind of studies.

Chapter 1 was devoted to some fundamentals about the nuclear shell model. We introduced the concept of isospin, as suggested by experimental observations of the property of the nuclear potential to be *almost* charge-symmetric and charge-independent. In fact experiments have shown that isospin non-conserving interaction can not be explained only by electromagnetic effects. A powerful tool to investigate the isospin breaking effects are the energy differences between isobaric analogue states of mirror nuclei (MED). These represent the ultimate goal of the analysis of this experiment.

A detailed description of the experimental apparatus was given in Chapter 2, while in Chapter 3 all the steps we followed during the data analysis were detailed. In particular, after having checked the consistency and calibration of the data, we obtained the particle identification matrix for the incoming secondary beam in BigRIPS and for the reaction products in ZeroDegree. We obtained the efficiencies of the detectors placed through the beamline and selected the most efficient combination of beam tracking detectors to be used in the following analysis. We checked also that the flux of the various nuclei populated was constant during the experiment, as shown in Figure 3.15 for the incoming ^{57}Zn in BigRIPS.

Finally the DALI2+ calibration was discussed. For the three sets of cali-

bration runs energy resolution, gain drift and the dependence of the FWHM on the energy was checked. We studied also the background which affected the scintillator detectors, finding two main peaks that influence the source spectra: the first decaying peak at 1293 keV is clearly a footprint of the presence of ^{41}Ar , while the second can be attributed to the decay of ^{40}K which is a natural background source. The study of the background is an important step for the calculations of the DALI2+ detectors efficiencies. The measurement of the array detector efficiencies will be one of the further steps of this analysis.

In Chapter 4 we reported the results obtained from the analysis. We mostly focused on the estimation of inclusive cross-sections. New estimates were obtained not only for the most exotic proton-rich nuclei, but for all the isotopes that were populated during the experiment. In particular the value of 9.3(7)(13) mbarn obtained for the one-neutron knockout from ^{57}Zn implies that a reduction factor of 0.4 is needed to theoretical estimations based on a eikonal model for the reactions and on the shell model for the single-particle strengths. This factor is coherent with systematics presented in Ref. [36]. Whenever data were available we compared the obtained cross-section values with literature, to test the consistence of the obtained results. For all the cases we found only small differences with our estimations.

In particular, we found a systematic increase of the inclusive one-neutron cross-sections estimates when the proton separation energy of the reaction products increases, indicating an higher density of states which can be populated in the ejectiles as we move towards less exotic proton-rich nuclei. We observed also a systematic enhancement between inclusive one-neutron and one-proton cross-sections for the same projectile that can be interpreted as the trend of nuclei to move towards a more stable configuration reducing their neutron-proton asymmetry.

Finally we briefly introduced the analysis of the gamma radiation emitted from the reaction products. Doppler-correction was first studied using known transitions, in particular we obtained the $4^+ \rightarrow 2^+$ and the $2^+ \rightarrow 0^+$ transitions in both ^{54}Fe and ^{52}Fe . Then, we reported the γ -spectra observed in coincidence with ^{55}Cu and ^{56}Cu populated respectively from the one-neutron knockout from ^{56}Cu and from the one-proton knockout from ^{57}Zn .

These preliminary results constitute the basis for the next step of the analysis. Many of the gamma transitions observed are expected to be retarded by non-negligible lifetime effects. As a consequence GEANT4 simulations of the lineshapes and the estimate of DALI2+ detectors efficiencies will be the next step. They will give us the energy values of the observed gamma transitions in ^{55}Cu and ^{56}Cu . With sufficient precision to enable the comparison of these energies with the energy of their isobaric analogue states in

the mirror nuclei which are ^{55}Fe and ^{56}Co respectively. A further analysis will obtain estimations on exclusive cross-sections, that, through comparison to shell model calculations, will provide understanding about structure and isospin symmetry violation for these exotic isotopes.

Bibliography

- [1] E. Rutherford. ‘LXXIX. The scattering of α and β particles by matter and the structure of the atom’. In: *The London, Edinburgh, and Dublin Philosophical Magazine and Journal of Science* 21.125 (1911). Ed. by Taylor & Francis, pp. 669–688.
- [2] J. J. Thomson. ‘XXIV. On the structure of the atom: an investigation of the stability and periods of oscillation of a number of corpuscles arranged at equal intervals around the circumference of a circle; with application of the results to the theory of atomic structure’. In: *The London, Edinburgh, and Dublin Philosophical Magazine and Journal of Science* 7.39 (1904). Ed. by Taylor & Francis, pp. 237–265.
- [3] W. M. Elsasser. ‘Sur le principe de Pauli dans les noyaux-III.’ In: *Journal de Physique et le Radium* 5.12 (1934). Ed. by Société Française de Physique, pp. 635–639.
- [4] K. Guggenheimer. ‘Remarques sur la constitution des noyaux atomiques-I.’ In: *Journal de Physique et le Radium* 5 (1934).
- [5] K. Heyde. *Basic ideas and concepts in nuclear physics: an introductory approach*. CRC Press, 2004.
- [6] M. G. Mayer. ‘On closed shells in nuclei. II’. In: *Physical Review* 75.12 (1949). Ed. by APS.
- [7] O. Haxel, J. H. D. Jensen, and H. E. Suess. ‘On the " magic numbers " in nuclear structure’. In: *Physical Review* 75.11 (1949). Ed. by APS.
- [8] W. Heisenberg. ‘Über den Bau der Atomkerne.’ In: *I. Z. Physik* 77 (1932). DOI: <https://doi.org/10.1007/BF01342433>.
- [9] K. S. Krane, D. Halliday, et al. *Introductory nuclear physics*. 1987.
- [10] J. A. Nolen Jr. and J. P. Schiffer. ‘Coulomb energies’. In: *Annual Review of Nuclear Science* 19.1 (1969), pp. 471–526.

- [11] M. A. Bentley and S. M. Lenzi. ‘Coulomb energy differences between high-spin states in isobaric multiplets’. In: *Progress in Particle and Nuclear Physics* 59.2 (2007). Ed. by Elsevier, pp. 497–561.
- [12] E. P. Wigner. ‘Proceedings of the Robert A. Welch Foundation Conference on Chemical Research’. In: (1957). Ed. by Texas Robert A. Welch Foundation Houston.
- [13] Y. Blumenfeld, T. Nilsson, and P. Van Duppen. ‘Facilities and methods for radioactive ion beam production’. In: *Physica Scripta* 2013.T152 (2013).
- [14] J. Cornell. ‘Radioactive ion beam facilities in Europe: current status and future development’. In: *17th International Conference on Cyclotrons and their Applications*. 2004.
- [15] A. C. Mueller. ‘An overview of radioactive beam facilities’. In:
- [16] T. Motobayashi. ‘World new facilities for radioactive isotope beams’. In: *EPJ Web of Conferences*. Vol. 66. EDP Sciences. 2014.
- [17] RIBF website. URL: <http://www.nishina.riken.jp/RIBF/accelerator/concept.html>.
- [18] Y. Shimizu et al. ‘SAMURAI project at RIBF’. In: *Journal of Physics: Conference Series*. 312 vols. 5. 2011.
- [19] J. D. Bowman, W.J. Swiatecki, and C. F. Tsang. ‘LBL-2908’. In: *unpublished report* (1973).
- [20] G. D. Westfall et al. ‘Nuclear fireball model for proton inclusive spectra from relativistic heavy-ion collisions’. In: *Physical Review Letters* 37.18 (1976), p. 1202.
- [21] H. Okuno, N. Fukunishi, and O. Kamigaito. ‘Progress of RIBF accelerators’. In: *Progress of Theoretical and Experimental Physics* 1 (2012), p. 03C002.
- [22] T. Kubo et al. ‘BigRIPS separator and ZeroDegree spectrometer at RIKEN RI Beam Factory’. In: *Progress of Theoretical and Experimental Physics* 2012.1 (2012).
- [23] T. Ohnishi et al. ‘Identification of new isotopes ^{125}Pd and ^{126}Pd produced by in-flight fission of 345 MeV/nucleon ^{238}U : first results from the RIKEN RI beam factory’. In: *Journal of the Physical Society of Japan* 77.8 (2008).

-
- [24] K. H. Schmidt et al. ‘The momentum-loss achromat—A new method for the isotopical separation of relativistic heavy ions’. In: *Nuclear Instruments and Methods in Physics Research Section A: Accelerators, Spectrometers, Detectors and Associated Equipment* 260.2-3 (1987).
- [25] G. F. Knoll. ‘Radiation Detection and Measurement, John Wiley & Sons’. In: *Inc., New York* (2000).
- [26] N. Fukuda et al. ‘Identification and separation of radioactive isotope beams by the BigRIPS separator at the RIKEN RI Beam Factory’. In: *Nuclear Instruments and Methods in Physics Research Section B: Beam Interactions with Materials and Atoms* 317 (2013). Ed. by Elsevier, pp. 323–332.
- [27] H. Kumagai et al. ‘Development of parallel plate avalanche counter (PPAC) for BigRIPS fragment separator’. In: *Nuclear Instruments and Methods in Physics Research Section B: Beam Interactions with Materials and Atoms* 317 (2013). Ed. by Elsevier, pp. 717–727.
- [28] M. L. Cortés Sua. ‘Inelastic scattering of Ni and Zn isotopes off a proton target’. PhD thesis. Technische Universität Darmstadt, 2016.
- [29] K. Kimura et al. ‘High-rate particle identification of high-energy heavy ions using a tilted electrode gas ionization chamber’. In: *Nuclear Instruments and Methods in Physics Research Section A: Accelerators, Spectrometers, Detectors and Associated Equipment* 538.1-3 (2005). Ed. by Elsevier, pp. 608–614.
- [30] A. Jhingan et al. ‘TEGIC: Concept and.. design parameters of a detector for beam species identification at FAIR-NUSTAR’. In: *DAE Symp. Nucl. Phys.* 63 (2018).
- [31] I. Murray et al. ‘DALI2+ at the RIKEN Nishina Center RIBF’. In: ().
- [32] H. N. Liu et al. ‘How Robust is the N= 34 Subshell Closure? First Spectroscopy of Ar 52’. In: *Physical review letters* 122.7 (2019). Ed. by APS.
- [33] S. Takeuchi et al. ‘DALI2: A NaI (Tl) detector array for measurements of γ rays from fast nuclei’. In: *Nuclear Instruments and Methods in Physics Research Section A: Accelerators, Spectrometers, Detectors and Associated Equipment* 763 (2014). Ed. by Elsevier, pp. 596–603.
- [34] P. G. Hansen and J. A. Tostevin. ‘Direct reactions with exotic nuclei’. In: *Annual Review of Nuclear and Particle Science* 53.1 (2003), p. 219.

-
- [35] A. Gade et al. ‘Reduction of spectroscopic strength: Weakly-bound and strongly-bound single-particle states studied using one-nucleon knockout reactions’. In: *Physical Review C* 77.4 (2008). Ed. by APS.
- [36] J. A. Tostevin and A. Gade. ‘Systematics of intermediate-energy single-nucleon removal cross sections’. In: *Physical Review C* 90.5 (2014). Ed. by APS.
- [37] V. Vaquero Soto. ‘Espectroscopia de rayos gamma en haz en la región alrededor del núcleo doblemente mágico ^{132}Sn ’. PhD thesis. Universidad Autónoma de Madrid, 2018.
- [38] L. Olivier. ‘Nuclear structure in the vicinity of ^{78}Ni : in-beam γ -ray spectroscopy of ^{79}Cu through proton knockout’. PhD thesis. Université Paris-Saclay, 2017.
- [39] M. Lettmann. ‘Spectroscopy of neutron-rich germanium and krypton isotopes-A quest of triaxiality’. PhD thesis. TUprints, 2018.
- [40] M. Spieker et al. ‘One-proton and one-neutron knockout reactions from $N=Z=28$ ^{56}Ni to the $A=55$ mirror pair ^{55}Co and ^{55}Ni ’. In: *Physical Review C* 99.5 (2019). Ed. by APS.
- [41] M. Spieker et al. ‘Experimental identification of the $T=1$, $J\pi=6+$ state of ^{54}Co and isospin symmetry in $A=54$ studied via one-nucleon knockout reactions’. In: *Physical Review C* 100.6 (2019). Ed. by APS.
- [42] K. L. Yurkewicz et al. ‘One-neutron knockout from ^{57}Ni ’. In: *Physical Review C* 74.2 (2006).
- [43] A. A. Valverde et al. ‘High-Precision Mass Measurement of ^{56}Cu and the Redirection of the r p-Process Flow’. In: *Physical Review Letters* 120.3 (2018).
- [44] M. Wang et al. ‘The AME2016 atomic mass evaluation (II). Tables, graphs and references’. In: *Chinese Physics C* 41.3 (2017).
- [45] N. Paul et al. ‘Prominence of Pairing in Inclusive (p, 2p) and (p, pn) Cross Sections from Neutron-Rich Nuclei’. In: *Physical review letters* 122.16 (2019).
- [46] R. Dirk. ‘Experiment Proposal, RIBF NP-PAC-17’. 2016.
- [47] E. Caurier and F. Nowacki. ‘Present status of shell model techniques’. In: *Acta Physica Polonica B* 30 (1999).
- [48] A. Poves et al. ‘Shell model study of the isobaric chains $A=50$, $A=51$ and $A=52$ ’. In: *Nuclear Physics A* 694.1-2 (2001).
- [49] C. Iliadis. *Nuclear physics of stars*. Ed. by John Wiley & Sons. 2015.

- [50] M. J. Taylor et al. ‘Spectroscopy of nuclei approaching the proton drip-line using a secondary-fragmentation technique with the RISING detector array’. In: *Journal of Physics G: Nuclear and Particle Physics* 31 (2005).
- [51] *ENSDF*. URL: <https://www.nndc.bnl.gov/ensdf/>.
- [52] H. J. Wollersheim et al. ‘Rare ISotopes INvestigation at GSI (RISING) using gamma-ray spectroscopy at relativistic energies’. In: *Nuclear Instruments and Methods in Physics Research Section A: Accelerators, Spectrometers, Detectors and Associated Equipment* 537.3 (2005).
- [53] E. Hagberg et al. ‘Beta decays of ^{44}V and ^{52}Co ’. In: *Nuclear Physics A* 613.3 (1997).

Acknowledgements

I would like to express my deep and sincere gratitude to my thesis supervisor, Dr. Francesco Recchia, for giving me the opportunity to take part in this analysis. I deeply appreciated all of the suggestions, feedbacks, continuous support I was provided with and the high level of trust in my capabilities.

I would like to thank my tutor, Dr. Liliana Cortés. I am extremely grateful for your assistance and suggestions throughout this work. I really appreciated all your help, your kindness and your positive attitude. I learned a lot from your experience and I had great time at Legnaro during the analysis.

Vorrei ringraziare i miei attuali ed ex-conquilini, Filippo, Stefano, Miriam, Nicolò, Nicola, Nicolas, Giordano, Julian, Penny e Marta, per questi tre bellissimi anni. Per avermi supportato e soprattutto sopportato durante questo percorso. Grazie per tutte le risate e per farmi sentire come se fossi a casa.

Grazie ad Andrea ed alle mie care amiche Gaia, Alice ed Elena per essere stati sempre presenti anche nella lontananza, per il loro affetto e indispensabile supporto.

Grazie alla mia super sorella Martina. Apprezzo davvero la tua cieca fiducia in me, il tuo affetto indiscusso e soprattutto il tuo incessante sostegno.

Ringrazio Lorenzo per essermi stato accanto, sempre. Soprattutto grazie per la tua infinita pazienza nei miei confronti, per il tuo indispensabile supporto e perché riesci sempre a farmi sorridere.

Infine ringrazio i miei genitori. Grazie per l'affetto che mi dimostrate, per il vostro supporto, per il vostro appoggio e per essere sempre presenti così da non farmi mai pesare la distanza.

